Characterization of the Gas-Liquid Interfacial Waves in Vertical Upward Co-current Annular Flows

J. L. Cuadros[1], Y. Rivera[1], C. Berna[1], A. Escrivá[1], J.L. Muñoz-Cobo[1], G. Monrós-Andreu[2], S. Chiva[2]

[1]Instituto Universitario de Ingeniería Energética
Universitat Politècnica de València (UPV)
Camino de Vera 14, 46022 Valencia (Spain)
Tel: +34 963879245
Emails: jocuaor@upv.es; yaridu@upv.es; ceberes@iie.upv.es; aescriva@iqn.upv.es; jlcobos@iqn.upv.es

[2] Department of Mechanical Engineering and Construction
Universitat Jaume I (UJI)
Av. de Vicent Sos Baynat, s/n,12071 Castelló de la Plana (Spain)
Emails: gmonros@uji.es; schiva@uji.es

ABSTRACT

For more than fifty years, hundreds of research works have focused on the study of annular flow because of its huge importance in many industrial processes, for instance, chemical, petroleum, etc., being of particular interest in nuclear industry. Specifically, interfacial waves play a vital role in the mass, momentum and energy transference processes between gas and liquid phases. This paper describes the new experimental measurements of vertical upward co-current two-phase gas-liquid flow carried out in a tube with an inner diameter of 44 mm. The liquid film thickness and the major characteristics of the interfacial waves have been measured using a non-intrusive instrument, a conductance probe. The physical phenomenon in which this device is based is the change in the electrical conductivity between air and water, i.e., the electrical signal collected in the sensor receiver depends on the thickness of the liquid film layer. The experimental measurements range from 2000 to 3500 l/min for the gas volumetric flow rate, and from 4 to 10 l/min for the liquid volumetric flow rate. Correlation of the experimental measurements of liquid film thickness and the major properties of the interfacial waves have been analyzed using non-dimensional numbers. An important part of the document focuses on the comparison of the experimental data and the fitting correlations against several of the most widely used expressions. Throughout this paper, in addition to present all the available correlations, the existing scattering found when comparing against other expressions have been also confirmed, underlining the existence of gaps of knowledge even today. Emphasize that the proposed correlations are the ones that better fit the data of all experimental series carried out under the present study for the analyzed variables, with almost all the experimental points covered by the ±10% error bands of the new correlations.

Keywords: Annular Flow; Vertical Upward Co-current Gas-Liquid Flow; Conductance Probe; Gas-Liquid Interface; Liquid Film and Disturbance Wave Properties; Empirical Correlation.

1. INTRODUCTION

Two-phase gas-liquid flow is one of the most important regimes that is commonly found in many different industrial equipment and applications, such as, petroleum, chemical, civil and nuclear industries. Concentrating on nuclear industry, two-phase flow appears in both, pressurized and boiling water reactors (PWRs and BWRs) [Lahey and Moody, 1993; Todreas and Kazimi, 1993; Kolev 2015]. In PWRs, annular flow can be shown under normal operation (for instance, in the secondary side of the steam generators) and under abnormal operation conditions (i.e., during accidental events, for instance, during LOCA accidents). While in BWRs, two-phase flows are present in the core region during normal operation and under off-normal operation conditions. In summary, the importance of two-phase flow in nuclear power plants (NPPs) has been proved, for both normal and abnormal operation, being of particular interest in safety analysis.

The distinct flow types are classified into many different classes, usually called flow patterns/regimes. The wide assortment of classifications is mainly caused by the subjective nature of the flow characterization methods. A map for vertical upward flow is displayed in Figure 1 [Berna et al., 2014].

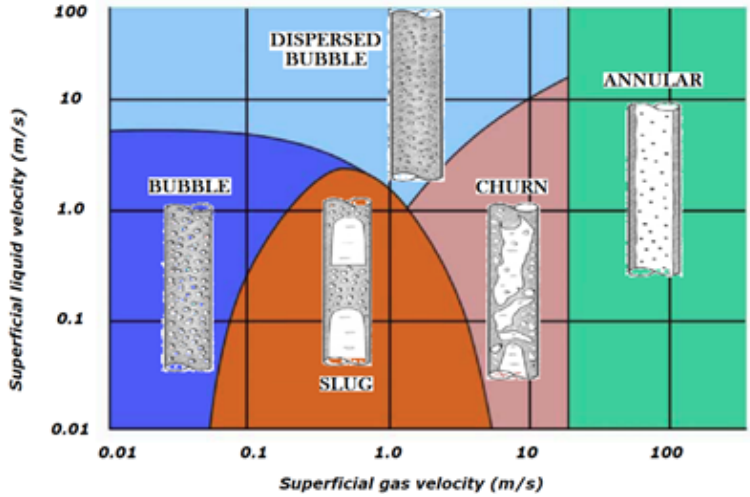

Figure 1. Flow map of vertical upward two-phase gas–liquid flow.

Annular flow is characterized by a thin adjacent ring of liquid in contact with the inner pipe wall and a gas phase flowing through its central region, usually with entrained droplets traveling within the gas phase [Dasgupta et al., 2017; Berna et al., 2015].Since the sixties is widely recognized that the gas-liquid interface is covered by a huge number of tridimensional waves [Hanratty and Hersman, 1961; Hall-Taylor et al., 1963; Wallis 1969; Hewitt and Hall-Taylor, 1970]. From that moment until now, all researchers explain that there are two different types of waves coexisting on the gas-liquid interface, the disturbance waves (DW) and the ripple waves (RW). DWs have longer lifetimes than RWs, also, DWs usually cover the whole tube ring and have an amplitude several times higher than the average liquid film thickness [Schubring and Shedd, 2008; Alekseenko et al., 2008 and 2009; Belt et al., 2010; Berna et al., 2014; Setyawan et al., 2016; Dasgupta et al., 2017]. While amplitude of RWs are much smaller than DWs', RWs have a short lifetime and are non-coherent. Both kinds of waves, along with their major related variables, are schematically displayed in Figure 2.

Over the past decades, only a limited number of studies have been focused on theoretical approaches of annular flow [Su et al., 2003a and 2003b; Kim and Mudawar, 2012 and 2014; Chen et al., 2015]. These theoretical models are based on fundamental conservation principles, the major flow variables are determined through numerically solving of the mass, energy and momentum conservation equations. While, the great majority of studies are focused on the characterization of the most important variables related with annular flows. In particular, the majority of them deal with the characterization of the gas-liquid interfacial waves' behavior, for both, horizontal and vertical flows. Gas-liquid interfacial waves play an important role in the entrainment process of droplets into the gas stream, also affecting significantly to the mass and heat transfer processes. Due to the major significance of the interfacial waves in the entrainment process, their adequate characterization is very important, particularly for the DW. Consequently, several variables must be determined: amplitude, frequency, celerity, etcetera. Along this paper, we will concentrate on the estimation of several of these major interfacial wave characteristics, mainly wave thickness, amplitude and frequency (Figure 2), all of them determined from the conductance probe measurements.

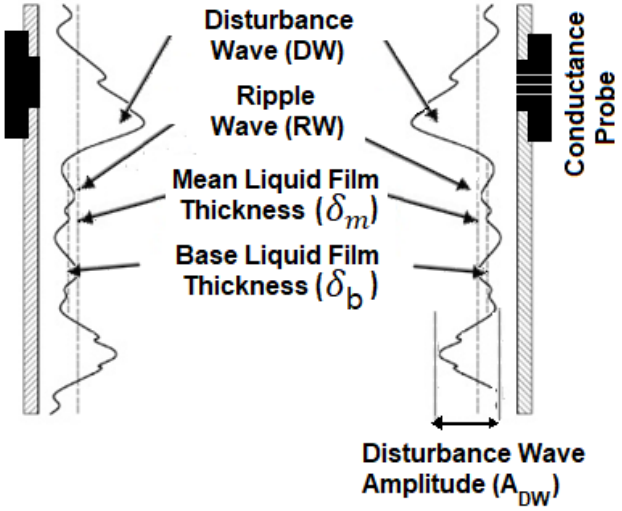

Figure 2. Schematic representation of the interfacial waves in annular flows and its major characteristics.

2. EXPERIMENTAL ARRANGEMENTS

2.1. General Description of the Experimental Facility

The VAFF facility (Vertical Annular Flow Facility) consists of an air-water loop, Figure 3. The major components of the facility are: the air pumping circuit, the water pumping system, the injector/mixer system, the test section and the air-water separator system. In all of these components, there are different sensors, in order to measure the main variables needed to determine the experimental conditions and to carry out further analysis.

The operation of the experimental facility is described below. The air is injected into the system through a compressor (maximum working pressure of 8 bars and a maximum volumetric flow rate of 3750 l/min). The air inlet volumetric

flow rate and pressure in the test section are controlled through two control valves. The water flow is driven by a water pump (with a maximum discharge pressure of 4.2 bars). The water is injected into the vertical pipe through a specific design pressurized water injector system, whose operating principle is based on the pressure difference between both sides of the component, so that water passes through a sintered stainless steel element. This two-phase mixture passes through the test section. Then, at the upper part of the facility, this gas-liquid mixture is separated through a centrifugal demisting cyclone. The air is vented to the atmosphere, while the water is returned back to a storage tank. The water storage tank is a large capacity plastic tank, from which the recirculation pump sucks the water and drives it to the injector system once again, in such a way that the water starts a new cycle. Whereas the air circuit is an open circuit, i.e., the air injected by the compressor is vented at the end of a working cycle to the surrounding atmosphere and fresh air from the compressor is injected back into the experimental facility.

The test section, in which the annular flow is studied, consists of a vertical methacrylate tube with an inner diameter of 44 mm and a total length between the water injection and the extraction systems of almost 5 meters. All the major experimental conditions are measured in this test section. Absolute pressure sensors, high accuracy differential pressure gauges and thermocouples are installed along this measurement section. In the upper part of the test section, at 4.7 m from the water inlet, an interfacial wave visualization port is installed (labeled as Probe in Figure 3).

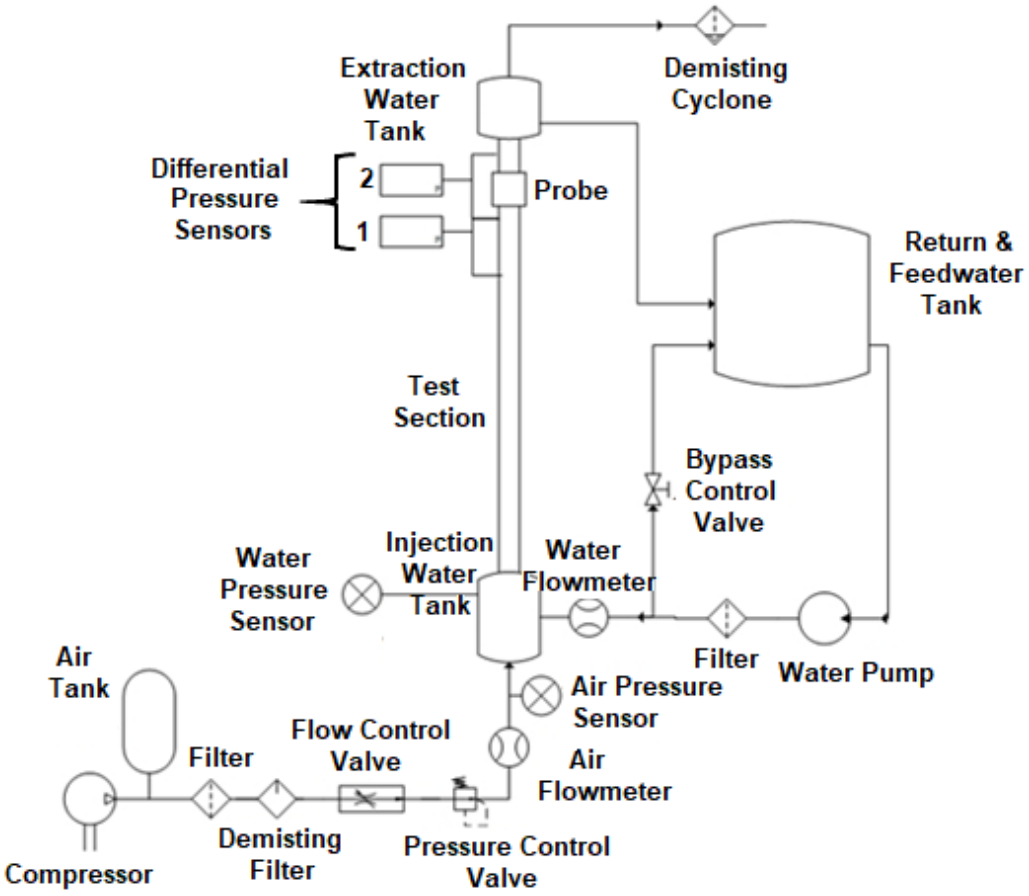

Figure 3. Schematic view of the VAFF facility.

2.2. The Water Injection System

The water injection system, shown in Figure 3, consists of a cylindrical annular tank, having in its central part the sintered stainless steel tube, a zoom of this component is displayed in Figure 4. The outer part of the injection system is pressurized (by the water pump), while its inner part remains approximately at ambient pressure (through which circulates the air stream). Since the sintered material has a pore size that allows the passage of water through it, the water volumetric flow rate is a function of the pressure difference between both sides. The water is able to pass through the pores of the sintered stainless steel due to the difference in pressure between the external and internal parts of this sintered material. The fundamental function of the sintered stainless steel tube is to bring into contact the low speed water and the high speed air stream, so that this contact takes place in the smoothest possible way.

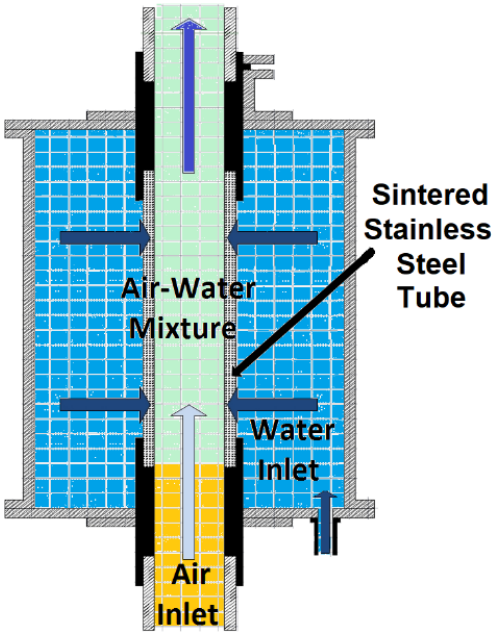

Figure 4. Schematic view of the water injector.

The operation principle of the water injection system is the empirical equation of Darcy (UNE-EN ISO 4022, 2007). In this equation, it is assumed that the pore size is big in comparison with the mean molecular distance of the working fluid (supposition which is true for all working fluids, except for low pressure or high temperature gases):

$$Q = \frac{\Delta P \, A \, \psi_s}{e \, \mu} \tag{1}$$

expression in which Q is the volumetric flow rate (m^3/s); e the material thickness in the perpendicular flow direction (m); μ the absolute or dynamic viscosity of the working fluid, defined by the Newton's law ($N \cdot s/m^2$); ΔP the difference in pressure between the inner and outer part of the sintered material (Pa); A the area of the porous medium in the normal direction of the flow (m^2), $A = \frac{\pi \, L \, d_{ext} \, Ln\left(\frac{d_{ext}}{d_{int}}\right)}{\frac{d_{ext}}{d_{int}} - 1}$; and ψ_s the coefficient of viscous permeability (m^2). The final conclusion of this water

injector system description is that the water volumetric flow rate introduced into the gas stream can be easily controlled. All variables in Eqn. (1) are constants for a determined sintered material and a working fluid, only the term of pressure can change, so that the water flow regulation is carried out by modifying the difference in pressure between the inner and outer surfaces of the sintered stainless steel.

2.3. Conductance Probe

The physical basis of the conductance sensors is the conductivity dependency with liquid layer thickness [Wayne, 2001; Tiwari et al., 2014; Muñoz-Cobo et al., 2017]. The conductance probe used in this experiment includes three electrodes, which are flush-mounted with the wall and aligned with the air and water flow directions. The first electrode is the transmitter, which carries a sinusoidal signal of 300 kHz and 4 Vpp. The central electrode is the ground connection. Finally, the third electrode is the receiver, which is responsible for the electric signal reception that was transmitted through the thin water layer. There is a proportionality between the film thickness and the signal received, which is caused by the correlation between the liquid film thickness and the number of electric field lines. Consequently, higher film thickness leads to higher number of electric field lines [Wayne, 2001].

The conductance probe has been built in Poly-Propylene (PPR), because of its mechanical properties. The port geometry has an inner diameter of 44 mm, equal to that of the test section, and a total length of 170 mm. The conductance sensor consists of 3 electrodes with 2 mm of inner diameter, spaced 1.5 mm between them. The electrodes, constructed by stainless steel, are located in the central part of the device (Figure 5).

Figure 5. View of the custom manufacturing port of the conductance probes.

The electronic circuit, whose flow diagram is schematically displayed in Figure 6, is designed to send, receive and amplify the electric signal. A part of the electronic circuit transmits the sine wave signal from a signal generator to the transmitter electrode, while the other part captures the signal coming from the receiver electrode. Then, the signal is rectified and filtered, in order to obtain a direct current signal proportional to the liquid film thickness. This value is acquired through a data acquisition card and, finally, it is stored in the computer for post-processing.

Figure 6. Flow diagram of the probe's electronic circuit performance.

The final step, before placing the conductance probe in the experimental facility, is the calibration procedure. The objective is to relate the voltage signal values with the water film thicknesses, i.e., to correlate the probe signal with the wavy liquid layer. The assembly configuration to perform the conductance probe calibration is displayed in Figure 7A. In this first calibration, the 3 electrodes were mounted on a flat surface, which allows the measurement of the fluid thickness at the micron level without affecting the surface tension. For the water used in the experiments (conductivity of 50μS), multiple measurements have been carried out, trying to optimize the frequency and voltage of the excitation signal, in order to obtain a sufficient voltage range in the measured signal, being the selected excitation signal a sinusoidal of 300 KHz and 4 Vpp. Finally, after having finished this optimization procedure, the definitive calibration process was carried out with the conductance probe used in the experiments and in a curved calibration device, Figure 7B. This device consists of three major components: a flatness table; an electronic precision positioning system; and several cylinders, with known diameter and made with a dielectric material; so that the dielectric cylinder is located at the desired position in the inner part of the conductance probe port, through the precision positioning system.

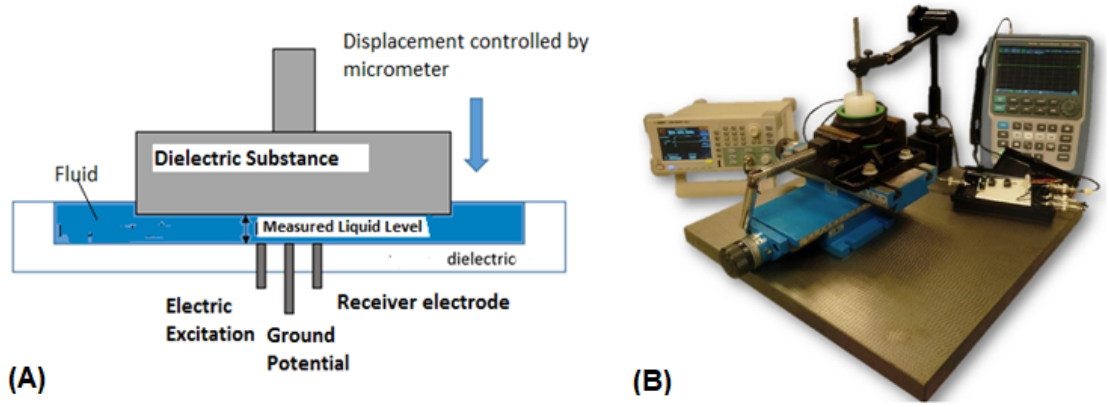

Figure 7. Calibration Devices of the Conductance Probes: (A) Flat; (B) Curved.

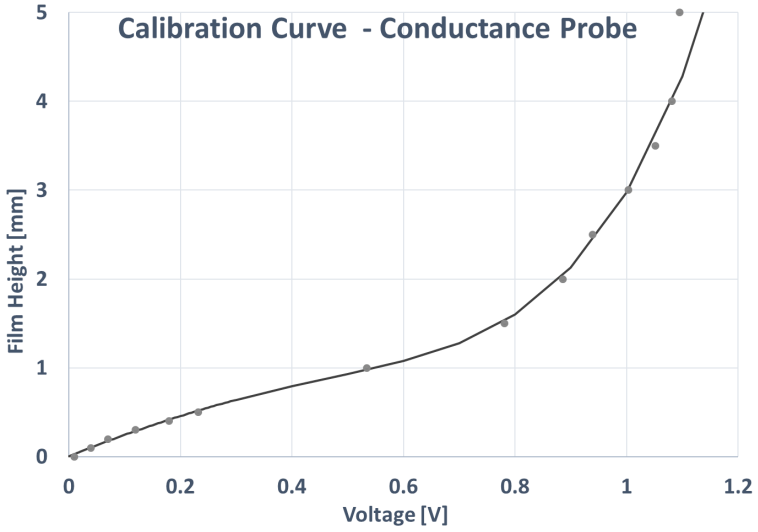

Figure 8. Calibration Points and Fitting Curve of the Conductance Probe.

Due to the operating characteristics of this type of sensors, not only conductivity but fluid temperature can be extremely important. However, for a

sufficiently narrow range of fluid conductivities and temperatures, the shape of the normalized voltage signal does not change appreciably. Figure 8 displays the calibration points and the fitted calibration curve of the probe that has been mounted in the experimental facility. This calibration procedure has been carried out with a curved calibration device in order to capture the possible curvature effects. The calibration curve was performed measuring at fourteen positions, i.e., fourteen different distances between the pipe wall and the dielectric cylinder wall. As previously mentioned, these measurements were carried out with the conductance probe used in the experimental series. The calibration procedure covered liquid layers ranges from 100μm to 5 mm, which lead to voltage measurements from 0.05 to 1.2 V approximately. For this range of values the conductance probe saturates, which means that has reached its maximum voltage value, i.e., the conductance probe becomes insensitive to further increases of the liquid layer. As can be seen in Figure 8, the calibration points and their fitting curve has a high correlation level, its mean squared deviation or error is MSD = 0.0035. Therefore, the way to obtain the liquid level (liquid film thickness) is to use the fitting curve function, which correlates the voltage measurements with the thickness of the liquid layer:

$$\delta(V) = 4.69 \cdot 10^{-3} - 5.42 \cdot V^{3.48} - 3.03 \cdot V^{0.96} + 6.24 \cdot V^{4.38} + 5.18 \cdot V^{0.95} \quad (2)$$

in which V is expressed in Volts and then the liquid film thickness is given in mm.

3. EXPERIMENTAL MEASUREMENTS

The test matrix consisted of forty-nine test runs, a total number of seven airflows and seven water flow values have been run during the experiment. In fact, ten water test runs were carried out, increasing liter by liter from 1 to 10 l/min (i.e., $1.67 \cdot 10^{-5}$-$1.67 \cdot 10^{-4}$ m^3/s), but continuity and stability of the thin liquid film layer could not be clearly appreciated for low liquid flow rate values. Consequently the final test matrix for the liquid flow rate covered from 4 to 10 l/min, while the air volumetric flow rate changed for the different runs between 2000 l/min to 3500 l/min (i.e., 0.0333 - 0.0583 m^3/s).

During the test runs, all the major experimental boundary conditions were monitored in real time, which include air and water volumetric flow rates, temperatures and pressures, along with the conductance probe measurements. The data acquisition system has been programmed in LabView, and distinguishes between two types of measurements: the most important one, i.e., the conductance probe measurements; and the rest of measurements. This acquisition system, for the conductance probe, records 10^5 samples per second (National Instruments PCI 6255 with 80 analogic channels and a maximum rate of 1.25 MS/s). While for the rest of experimental data, the acquisition system records 100 samples per second (National Instruments cDAQ-9174 chassis compactDAQ with a module NI 9207 of 16 analogic channels and a maximum rate of 500 S/s).

The procedure followed in each test run is the following:

- Adjustment of the air and liquid flows at the desired values.

- Check of the steadiness of the major experimental conditions (air and liquid flows, pressures, temperatures), through the signal monitoring in real time with the LabView program.

- Data collection, record of two data files during sixty seconds (one for the conductance probe with $6 \cdot 10^6$ points and another for the rest of data with 120 points for each variable).

3.1. Tests Boundary Conditions

The first group of boundary conditions are those related with pressure, temperature and volumetric flow rate, which have to remain constant during the experimental series. Furthermore, before starting each test, the steadiness of these major boundary conditions measurements has been verified (Figure 9).

The steadiness or unsteadiness of the flow depends on whether or not there are equilibrium conditions on the gas-liquid interface. Unstable flow conditions would probably be caused by one, or the combination of the two subsequent causes: the existence of an extremely thin liquid sheet, with un-wetted areas, i.e., liquid film discontinuities; and/or the entrained droplet fraction in the gas core is not constant, i.e., the entrainment-deposition processes have not reached the equilibrium conditions.

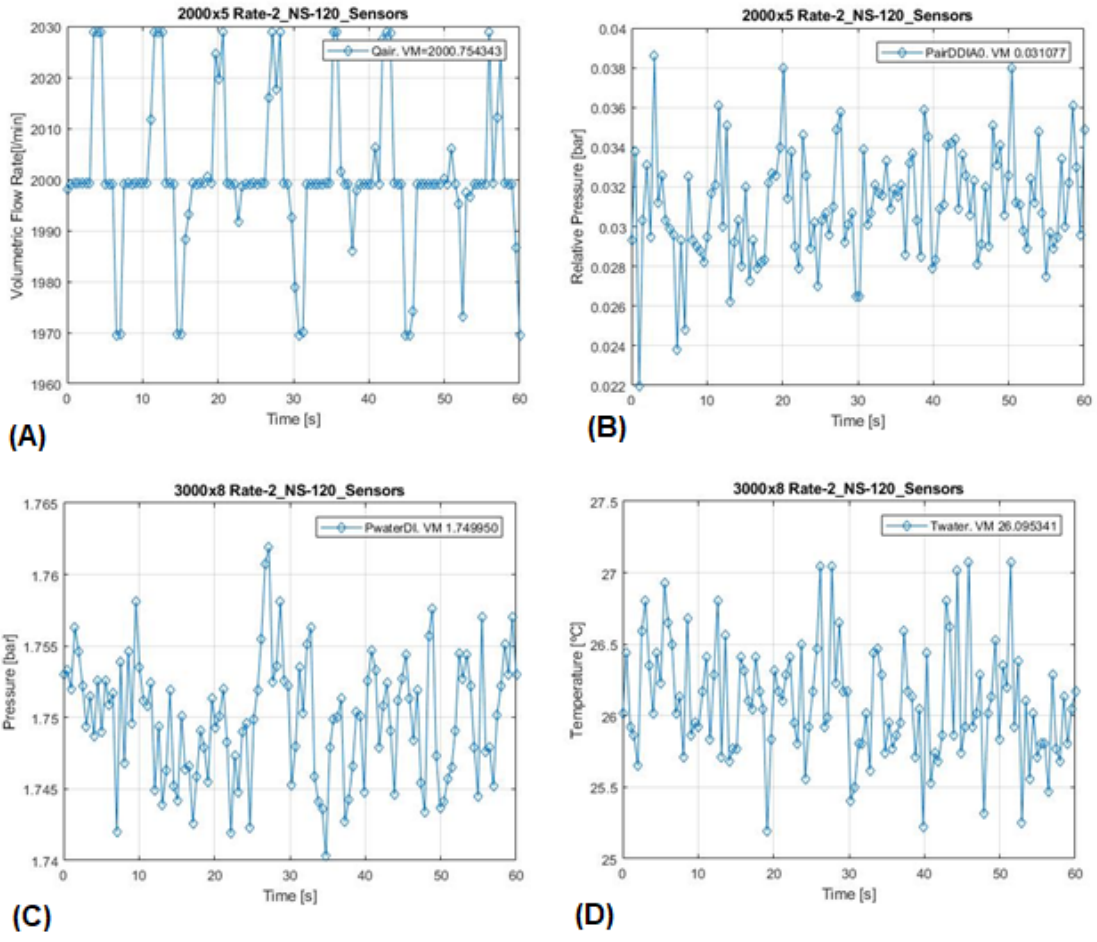

Figure 9. Examples of the experimental Boundary Conditions: (A) Air Volumetric Flow Rate; (B) Relative Pressure just before the test section; (C) Absolute Pressure into the Water Injection System; (D) Temperature into the Water Injection System.

As explained earlier, important pressure measurements have been carried out through the two differential transducers placed in the upper part of the facility (Figure 3 – Differential pressure sensors 1 and 2). The values provided by these two sensors give the answer to the degree of development of the flow (fully developed or under development). When the differential pressure remains constant between two pairs of points separated the same distance and placed at different test section position, then the flow is under fully developed conditions, Figure 10A. If the pressure difference is higher in the lower positioned pair of points than in the higher pair, the flow is under developing conditions, as shown in Figure 10B. The differential pressure measurements have shown to be mainly function of the liquid flow, stabilizing approximately for liquid flow rates over a threshold value. In our case, for the experimental range of gas flow rates covered in the study (from 2000 to 3500 l/min), the differential pressure measurements were not stabilized up to the moment in which values of liquid flow rates reached the 4 l/min. This threshold value was also slightly affected by the gas flow rate, i.e., lower gas flows leads to lower liquid flow threshold values too.

Consequently, if pressure gradients are not equal between two test section regions, the flow is considered to not be fully developed along these sections. Then, as it is widely recognized [Collier and Thome, 1994; Cioncolini and Thome, 2017], there are not stabilized conditions for low liquid flow rates, as shown comparing Figure 10A-B. Thus, as a conclusion, the volumetric liquid flow rate of the experimental series starts above the threshold value of 4 l/min.

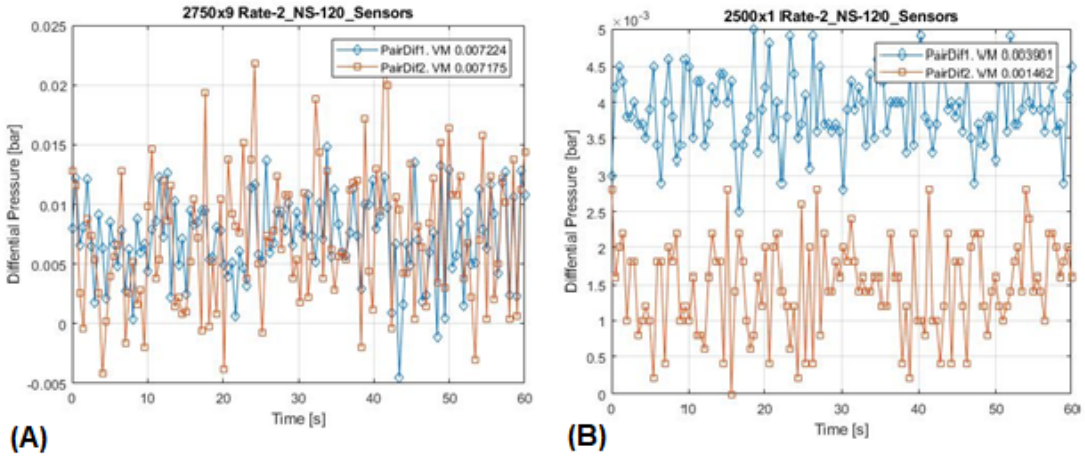

Figure 10. Measurements of lower and upper differential pressure transducers along the test section (PairDif.1 and PairDif.2 respectively): (A) test of Q_{air}= 2750 l/min and Q_{water}=9 l/min; (B) test of Q_{air}= 2500 l/min and Q_{water}=1 l /min.

3.2. The Conductance Probe

As mentioned in the previous section, the test matrix analyzed along this paper consist of forty-nine test runs (seven airflows and seven water flows), air volumetric flow rates from 2000 to 3500 l/min and water volumetric flow rates from 4 to 10 l/min. The pressure in the upper part of the facility was atmospheric, and the water and air temperatures were kept constant along each data series at about 25 and 30 ºC respectively.

The sixty seconds of the conductance probe raw data for the forty-nine experimental series were recorded, an example is plotted in Figure 11. Taking

the raw data as a starting point, a conditioning procedure is followed. First, the calibration fitting function was used to convert the raw signal in volts to film thickness in millimeters for all the experimental series, Eqn. (2) and Figure 8. Next, a signal conditioning procedure was applied to the pretreated data (voltage signal of the conductance probe converted to thickness). In particular, a Savitzky-Golay filter had been applied to the pretreated data points with the purpose of smoothing them, i.e., in order to increase the signal-to-noise ratio with the least distortion of the signal (Figure 12).

In order to become familiar with the influence of the variation of water and air flow rates in the liquid film thickness, a summary of one second measurements of nine tests, low-medium-high gas-liquid flow rates (volumetric air flow rates of 2000-2750-3500 l/min and volumetric water flow rates of 4-7-10 l/min) are shown in Figure 13. At a first glance, an increase in the wave amplitude is observed with the increase in the liquid flow rate, while a decrease in the wave amplitude is shown as the air flow rate become bigger. These tendencies, among other findings, will be analyzed in depth along later sections.

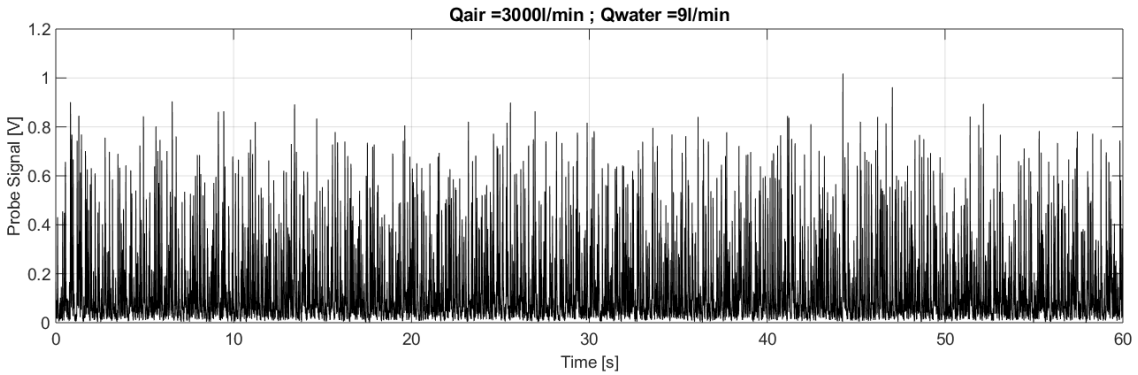

Figure 11. Raw conductance probe measurements in the test section for an air volumetric flow rate of 3000 l/min and a water volumetric flow rate of 9 l/min.

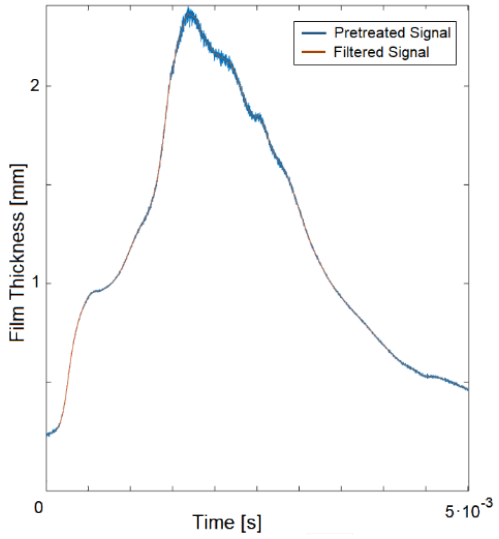

Figure 12. Zoom of $5 \cdot 10^{-3}$ seconds of the conductance probe measurements before and after signal filtering for an air volumetric flow rate of 2000 l/min and a water volumetric flow rate of 10 l/min.

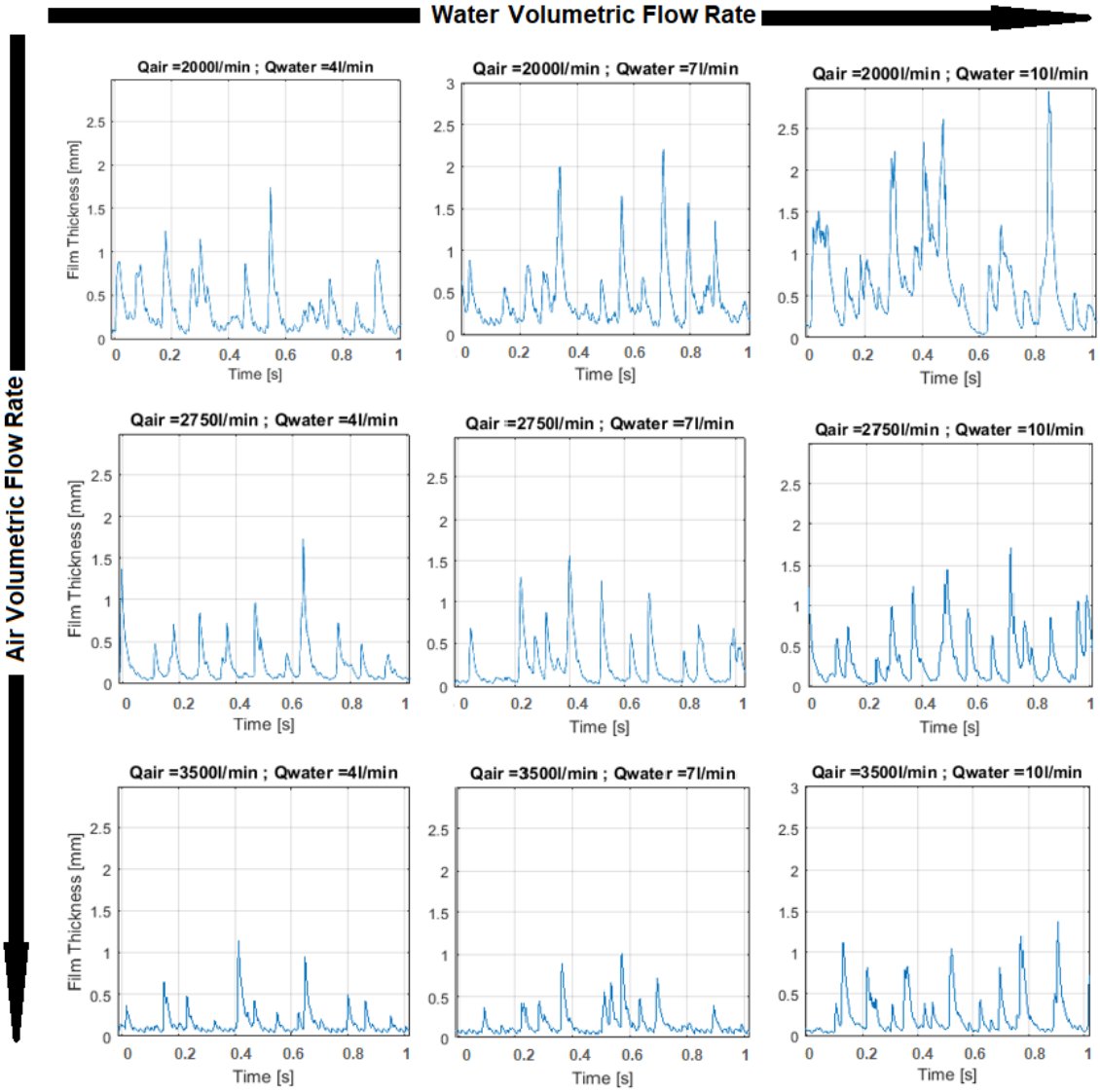

Figure 13. Comparison of a one second zoom of the conductance probe measurements (after raw signal filtering and conversion from voltage to thickness) in the test section for the extreme and central values of the air and water volumetric flow rates.

4. ANALYSIS OF THE CONDUCTANCE PROBE MEASUREMENTS

After the conditioning treatment of the raw conductance probe signals, in this section, the mean values of the major variables are shown. Specifically, for each of the 49 experimental series of 60 seconds each one, a series of average values of the main variables related to the characterization of interfacial waves have been obtained. In particular, a summary of all of them are shown along the current section. It should be highlighted that, from this moment on, all variables will be displayed in terms of superficial velocities instead of volumetric flow rates, because all adjustments will be carried out as function of these velocities. As it is well-known, superficial velocities are obtained by simply dividing the volumetric flow rate of each phase between the pipe section.

Mention that a possible error source could have been the degree of DWs incoherence along the pipe circumferential section. DWs' incoherence could be motivated by several causes, such as, pipe diameter, gas and/or liquid flow rates, etc. As explained by some researchers, the DWs incoherence along the tube circumference increases with pipe diameter [Sawant et al., 2008; Azzopardi, 1997]. Even though, other authors stress that circumferential coherence is one of the DWs major characteristics [Zhao et al., 2013; Dasgupta et al., 2017]. Zhao et al. observed this coherence along a length of 25-50 diameters in vertical upward annular flow in a pipe of an inner diameter of 34.5 mm. Several years before, Azzopardi conducted a detailed analysis of the interfacial waves' structure in vertical annular flows [Azzopardi, 1986]. The major conclusions of Azzopardi's work were that higher pipe diameters lead to higher DW incoherence, while high gas flow rates lead to less DW incoherence, having not effect the liquid mass flow rate on DWs' coherence. In any case, as our experimental measurements were recorded during a long interval of time, 60 seconds, a significant averaged value of the evolution of the different variables is obtained under fully developed flow conditions. Consequently, as our estimations come from averaging calculations over long periods of time, then all these circumferential effects are not a significant error source.

In summary, in order to estimate the errors of the experimental measurements for the test series, a repeatability trial has been made. A run test has been repeated ten times in between the rest of the experimental tests, in such a way that, assuming a normal probability distribution function, the error margin of a determined variable can be estimated through the following expression:

$$\pm \mathrm{Z}_{\alpha/2}\frac{\sigma}{\sqrt{n}} \tag{3}$$

where $Z_{\alpha/2}$ is the confidence coefficient which depends on the confidence level, which for the usual 95% has a value of 1.96; σ is the standard deviation; and n is the number of runs. Table 1 displays a summary of these calculations for the experimental values analysed along the present study.

As shown in the table, the repeatability study provides assumable errors for the four analyzed variables. Specifically, errors between ±1.62 and ±7.24, have been estimated, which seems quite logical. As can be seen at first glance, the measurements of the base film thickness have the lowest error value. While the wave characteristics (amplitude and frequency) are more variable than the base thickness. Consequently, these variables are more difficult to be accurately measured, particularly the amplitude of the DWs with the highest error values. Finally, the mean film thickness, which is obtained from the addition of mean value of the wave amplitudes to the base film thickness, results in an intermediate value of the error band.

Table 1. Summary of the Repeatability Analysis Results for the variables under study.

	δ_m (μm)	δ_b (μm)	A_{DW} (μm)	ν_{DW} (Hz)
σ	43.5	7.60	79.3	0.68
Error (%)	±5.67	±1.62	±7.24	±4.10

4.1. Liquid Film Thickness Measurements

Two variables related with the liquid film thickness have been estimated, these are the mean and base film thicknesses (δ_m and δ_b respectively), their summary test measurement data are displayed in Tables 2 and 3. The mean liquid film thickness can be defined as the distance from the pipe wall to the mean height of the waves produced in the gas-liquid interface. While the base film thickness is usually defined as the average liquid thickness value between two neighboring DW, i.e., mean value of the liquid layer without considering the DWs. As can be seen in both tables, and as could be intuitively thought-out, there is a decreasing tendency of both film thicknesses with the increase of air and water flow rates.

Table 2. Summary of the Mean Liquid Film Thickness (δ_m) in terms of Superficial Air and Water Flow Rates.

δ_m (μm) ↘ / Superficial Air Velocity (m/s) ↓	Superficial Water Velocity (m/s)						
	0.044	**0.055**	**0.066**	**0.077**	**0.088**	**0.099**	**0.11**
21.9	359	436	450	483	508	533	566
24.7	252	295	319	349	376	403	427
27.4	219	247	284	309	336	341	371
30.1	183	210	224	247	271	280	293
32.9	155	189	215	245	255	280	311
35.6	127	151	177	192	220	255	263
38.4	128	154	170	196	200	227	248

Table 3. Summary of the Base Liquid Film Thickness (δ_b) in terms of Superficial Air and Water Flow Rates.

δ_b (μm) ↘ / Superficial Air Velocity (m/s) ↓	Superficial Water Velocity (m/s)						
	0.044	**0.055**	**0.066**	**0.077**	**0.088**	**0.099**	**0.11**
21.9	200	230	247	266	266	278	280
24.7	135	162	181	199	211	222	233
27.4	133	151	173	180	190	196	201
30.1	103	120	137	146	162	166	173
32.9	99	118	136	153	152	166	177
35.6	75	93	109	121	137	153	160
38.4	85	103	116	133	130	146	154

Figure 14 is a 3D representation of the experimentally measured mean film thickness versus superficial air and water velocities, having a similar shape to

that of the base film thickness measurements. As shown in the figure, an increase of the water flow rate with constant air flow rate leads to an increase of the film thickness, while the increase of the air flow rate with constant liquid flow rate leads to a decrease of the liquid film thickness. These two tendencies can be visualized, even more clearly, by displaying the variation of the mean and base water film thicknesses versus superficial water velocity with constant superficial air velocity (Figure 15) and versus air flow rate with constant superficial water velocity (Figure 16).

A first analysis of these two variables leads to an important finding, which can be drawn directly from the experimental data of this study, i.e., a clear correlation between the mean and base liquid film thicknesses. Specifically, a linearity between the measurements for both variables and for all the studied experimental conditions, Figure 17. This correlation is as follows:

$$\delta_b = 0.473 \cdot \delta_m + 30.22 \tag{4}$$

in which both film thicknesses are expressed in micrometers. As displayed in Figure 17, there is a very good fitting of all the experimental data series, reaching a high value of the correlation coefficient, R^2=0.983. Detailed data analysis of both variables will be carried out throughout the results section, in which both variables will be correlated in terms of dimensionless numbers.

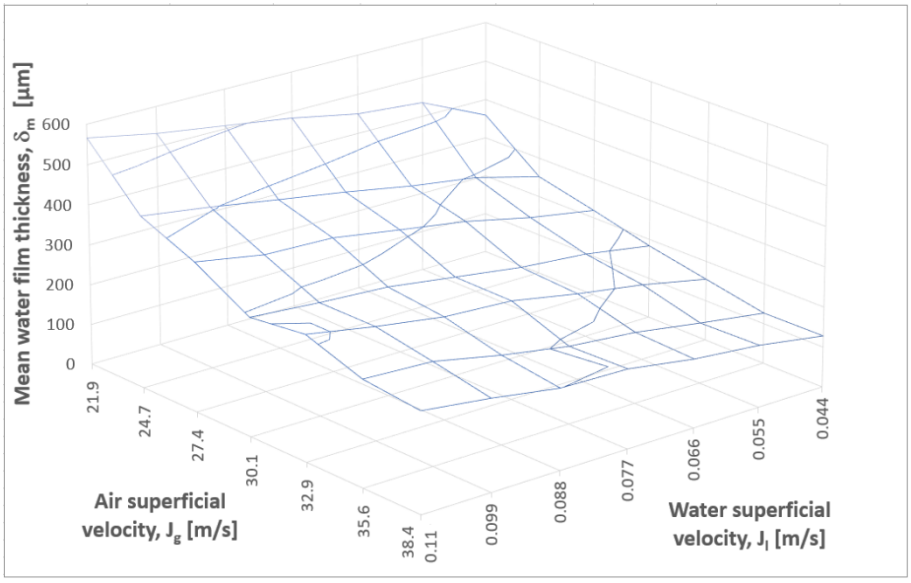

Figure 14. Mean Liquid Film Thickness versus Superficial Air and Water Velocities.

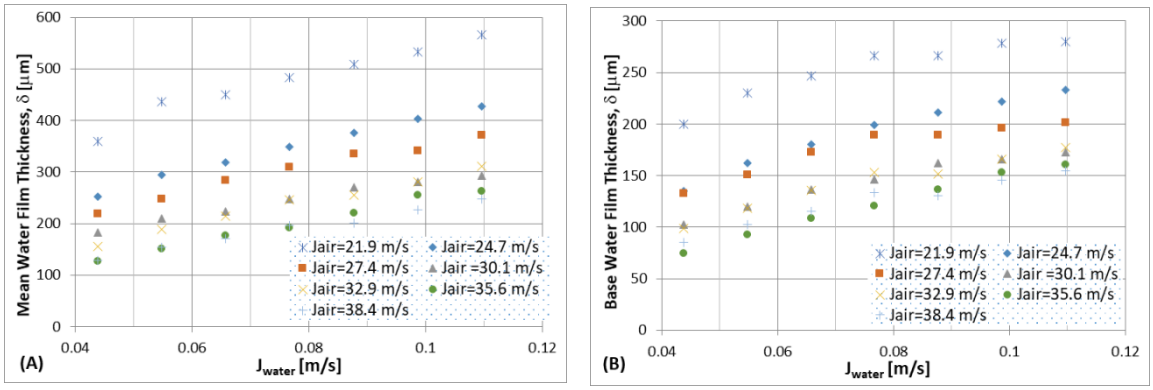

Figure 15. Liquid Film Thickness data vs. Superficial Water Velocity with constant superficial gas velocity: (A) Mean Water Film Thickness; (B) Base Water Film Thickness.

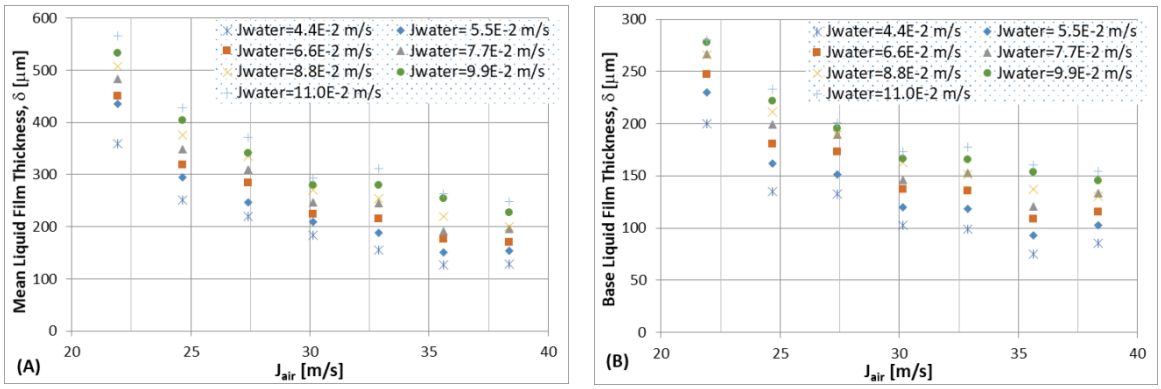

Figure 16. Liquid Film Thickness data vs. Superficial Air Velocity with constant water superficial velocity: (A) Mean Water Film Thickness; (B) Base Water Film Thickness.

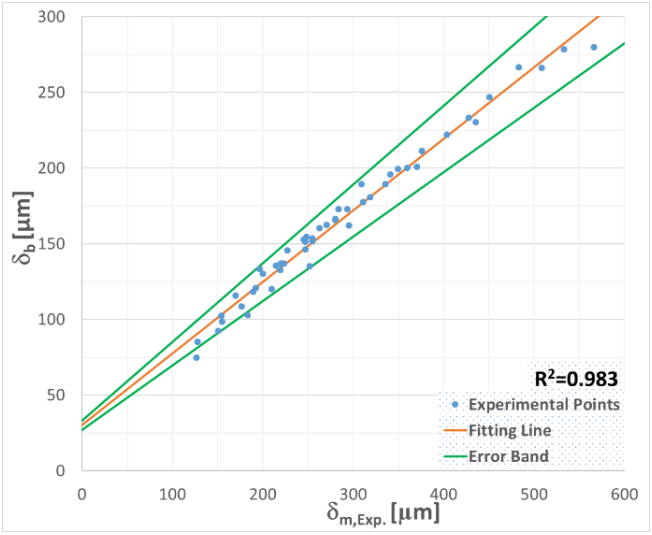

Figure 17. Correlation of the experimental measurements of the Base Water Film Thickness in terms of the Mean Liquid Film Thickness.

4.2. Disturbance Wave Measurements

Two major variables related with the large amplitude waves that appear on the gas-liquid interface, which are usually called disturbance waves (DWs), have been calculated along this section: the wave amplitude and frequency.

Prior to display the experimental data of these two DWs variables, the criteria used to identify them have to be defined. Several procedures to identify the DWs have been developed by different researchers over the past years. De Jong and Gabriel established a threshold value of the wave height as criterion to identify a wave as DW, specifically, when a portion of the time trace had a height exceeding the averaged value of the film thickness plus a standard deviation [De Jong and Gabriel, 2003]. In Rodriguez's thesis, he also defined a threshold value to identify the DWs, which was calculated adding to the mean base film thickness one and a half times its standard deviation [Rodríguez, 2004]. Belt et al. used a quite different criterion, which is based on the coherence of the DW versus the non-coherence of the remaining waves [Belt et al., 2010]. Paras and Karabelas used another way to define the DWs, the criterion was to identify the DWs as the ones with frequency similar to that of the dominant frequency of the power spectral density function [Paras and Karabelas, 1991]. While the criterion used in

the current work is to choose a threshold value too, as De Jong-Gabriel's and Rodríguez's criterion, but for us this is only the first cut off value, because we add other criteria to refine the identification procedure. This first threshold value depends on the base film thickness of the test under study. The next one is a closeness criterion, which has been implemented in order to avoid double peaks in wave crests. Finally, to discard low amplitude peaks located at intermediate points of large DWs a threshold value of relative amplitude is also applied. With this third criterion, the RWs that reach the DWs, those RWs formed on the DWs and those reached by the DWs are eliminated.

After the implementation of these DWs identification criteria, Table 4 and Figure 18 display the tendencies of the DWs' amplitude as function of the gas and liquid flow rates. As clearly shown in the table and figure, there is a marked downward trend of the DW amplitudes as the air flow rate increases. While the tendency is not so clear, when the water flow rate increases, the wave amplitude tends to grow.

Table 4. Summary of the Disturbance Waves Amplitude (A_{DW}) in function of Superficial Air and Water Velocities.

A_{DW} (μm) ↘ / Superficial Air Velocity (m/s) ↓	Superficial Water Velocity (m/s)						
	0.044	**0.055**	**0.066**	**0.077**	**0.088**	**0.099**	**0.11**
21.9	878	989	1014	1021	897	921	921
24.7	720	746	772	792	799	791	772
27.4	687	739	802	838	841	819	864
30.1	632	677	682	728	737	732	742
32.9	494	599	667	705	749	760	789
35.6	484	554	619	652	669	720	716
38.4	346	462	551	574	631	671	707

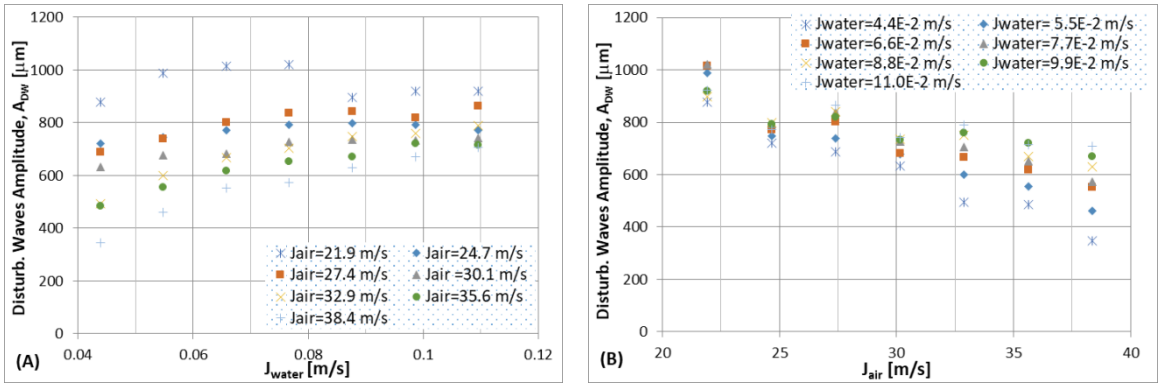

Figure 18. Disturbance Waves Amplitudes data in terms of the Superficial Fluid Velocities: (A) superficial water velocity with constant gas velocity; (B) superficial air velocity with constant superficial water velocity.

As explained in the previous paragraph, the wave amplitude depends mainly on gas velocities, which is clearly appreciated in this figure, being less

dependent on the total inlet water mass flow rate. However, there are differences in the influence of the water flow rate between the low and high air flows. At low air flow rates, there is less influence of the water flow in the DWs amplitude, and it increases with gas velocity. That is, there are appreciable differences in the values of the wave amplitudes at high superficial air velocities. For high gas flow rates, i.e., 32.9, 35.6 and 38.4 m/s the differences in the waves amplitudes are about 300-400 μm between the lowest and highest superficial liquid velocities ($4.4 \cdot 10^{-2}$and $11.0 \cdot 10^{-2}$ m/s respectively). However, for the lower values of the air velocity (21.9, 24.7, 27.4 and 30.1 m/s), the differences between the lowest and highest liquid velocities in the amplitudes of the DWs barely reach 100-150 μm.

Another qualitative dependency is the existent between the mean liquid film thickness and the amplitude of the DWs, as displayed in Figure 19. Thin liquid layers lead to small amplitudes of the DWs, while thicker layers of liquid lead to larger DWs amplitudes. Which implies that the values of the mean liquid film thickness are proportional to the liquid flow rate and inversely proportional to the gas flow rates. Then, the smallest DWs amplitudes have been measured for the lowest values of liquid flow rates and highest values of gas flow rates. While, in contrast, the largest DWs amplitudes have been measured for the highest values of liquid flow rates and lowest values of gas flow rates.

In order to have a first idea of the DWs amplitude evolution as function of the mean liquid film thicknesses, a first qualitative approach in form of a correlation has been carried out. The proposed correlation is as follows:

$$A_{DW} = 3.544 \cdot 10^2 \, Ln\left(\frac{\delta_m}{L_{interf}}\right) + 1.553 \cdot 10^3 \qquad (5)$$

in which the mean liquid film thickness has been non-dimensionalized by dividing by L_{interf}, which is the characteristic length in the interface stability theory, defined by $L_{interf} = \sqrt{\frac{\sigma}{g \cdot \rho_l}}$. The DW amplitudes have been correlated as function of the mean liquid film thickness through this dimensionless film thickness, being A_{DW} given in micrometers. As displayed in Figure 19, there is a quite good fitting of all the experimental data series, reaching a reasonable value of the correlation coefficient, R^2=0.883.

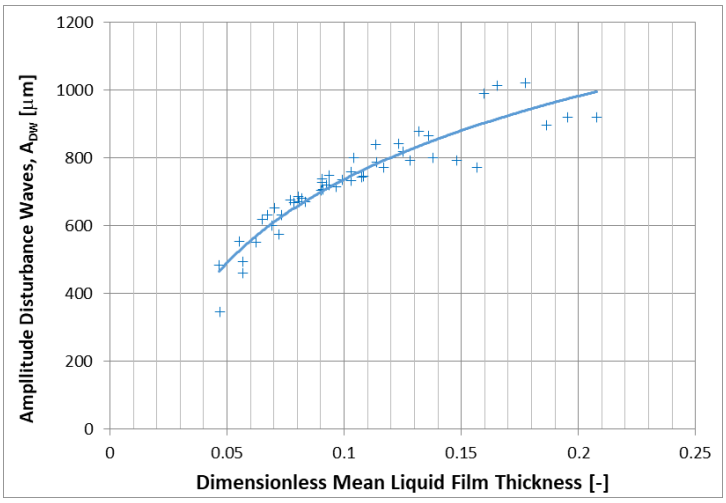

Figure 19. Experimental measurements of the Disturbance Wave Amplitudes of the as function of the Dimensionless Mean Water Film Thicknesses.

Table 5 and Figure 20 display the tendencies of the DW frequency as function of the superficial gas and liquid velocities. The frequency range covered in the current experiments is fairly narrow, between 8 and 18 Hz approximately, but despite this narrowness of the DW frequency range, there is a clear increasing tendency with superficial liquid velocity. In addition, an upward trend with the increase of the superficial gas velocity has also been observed. Both comments are made with reservations, taking into account the narrow frequency range covered in the experimental measurements and considering the existence of several experimental points in which the mentioned trends are not followed by the experimental measurements. Taking into account that there are different opinions with regard to the influence factors on the DW frequencies. The moderate increase in the wave frequency with both, gas and liquid flow rates, shown in Table 5 and Figure 20 are in the same line than recent publications [Dasgupta et al., 2017]. Other researchers state that wave frequency is proportional to liquid flow rate and independent of gas flow rate [Han et al., 2006; Hall-Taylor et al., 1963]. While other researchers predict a higher influence of the gas velocity in the DW frequencies [Setyawan et al., 2016; Paras and Karabelas, 1991]. Summarizing, wave frequency measurements is a quite challenging task, not to count the waves but the criteria used to classify and group the waves. Consequently, a large scattering has been found in the experimental data of the different researcher's works [Setyawan et al., 2016; Berna et al., 2014; Schubring, 2009; Paras and Karabelas, 1991].

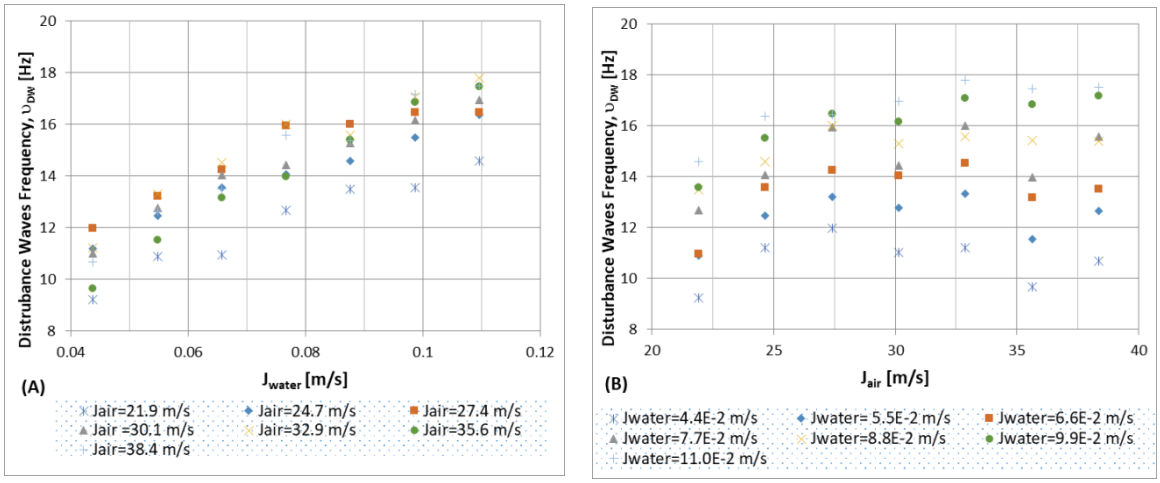

Figure 20. Disturbance Waves Frequency data as function of the Superficial Fluid Velocities: (A) superficial water velocity with constant gas velocity; (B) superficial air velocity with constant superficial water velocity.

Table 5. Summary of the Disturbance Wave Frequencies (ν_{DW}) in function of Superficial Air and Water Velocities.

ν_{DW} (Hz)		Superficial Water Velocity (m/s)						
		0.044	**0.055**	**0.066**	**0.077**	**0.088**	**0.099**	**0.11**
Superficial Air Velocity	**21.9**	9.23	10.88	10.95	12.67	13.48	13.57	14.58
	24.7	11.20	12.47	13.57	14.07	14.58	15.50	16.38
	27.4	11.97	13.22	14.25	15.95	16.00	16.47	16.45

	30.1	11.02	12.77	14.05	14.43	15.28	16.17	16.95
	32.9	11.22	13.32	14.52	16.02	15.58	17.08	17.78
	35.6	9.65	11.53	13.17	13.98	15.42	16.85	17.47
	38.4	10.68	12.65	13.50	15.83	15.38	17.17	17.50

5. RESULTS: ANALYSIS, COMPARISON AND DISCUSSION

This section is mainly devoted to develop the detailed adjustment procedure of the experimental measurements presented in the previous section. Several correlations to characterize the water film thicknesses have been developed. Specifically, we have focused on the estimation of the mean liquid film thickness, base film thickness and amplitude of the large amplitude interfacial waves (Disturbance Waves, DWs). Thus, we have made a division into two sections, one related with all the calculations of the film thickness (mean and base thicknesses) and the other related with calculations of the DW properties (amplitudes and frequencies). Finally, each one has been divided into two subsections, in which the calculations of each variable have been carried out. All subsections are arranged in the same manner: first, we show the empirical correlations, which have been worked out from the experimental data; and finally, we display the comparison of the new correlations estimations against several well-known correlations, all of them for our experimental data.

As far as the procedure to correlate these variables is concerned say that, as it is widely recognized, several different flow regimes are possible when a gas flows over a liquid film. The existing regime mainly depends on the difference in velocity between both phases. Consequently, as suggested by several authors [Ishii and Grolmes, 1975; Berna et al., 2014; Pan et al., 2015], the characteristics of the gas-liquid interface are expected to be consequence of a continuous force balance. From one side, the forces that try to maintain a smooth surface (viscosity or surface tension forces) and, on the other side, the forces that try to disturb this flat surface (inertial forces). This equilibrium of forces finally leads to a dependency between the difference in velocity of the gas and liquid phases and the aforementioned characteristics. Particularly, the annular flow is characterized by a high gas/liquid velocity ratio, it begins when gas velocity is about an order of magnitude higher than liquid velocity. Consequently, as dimensionless numbers dependency on these balance forces have been widely used during the last decades, then in order to characterize all variables related with the gas-liquid interface, this has been the methodology used. Specifically, the gas and liquid Reynolds numbers, the Weber number, gas and liquid Froude numbers have been tested, due to the fact that are the most frequently used in many research works. Among them, both Reynolds numbers have proved to be more than enough to reach good fitting of the variables under study. In addition to these dimensionless numbers, the Strouhal number has been used to characterize the DWs' frequency behavior.

5.1. Analysis of the Liquid Film Thickness

5.1.1. MEAN LIQUID FILM THICKNESS

One of the most important variables needed to characterize the liquid film in annular flow is the mean liquid film thickness, which can be defined as the distance from the pipe wall to an average height of the gas-liquid interface waves (Figure 2). The procedure followed to study this variable consists in the development of a new correlation with the experimental data and, then, the comparison of the experimental data against the new correlation and against other widely used correlations.

5.1.1.1. Correlation of the Mean Liquid Film Thickness

Our experimental values of the mean liquid film thickness have been correlated as function of the experimental conditions. The correlation of the mean liquid film thickness has been made through the adjustment of the experimental data versus the physical properties and boundary conditions. In order to have a more general relationship, we have taken the corresponding dimensionless numbers as variables for the adjustment. Therefore, the new correlation obtained is

$$\frac{\delta_m}{D} = 9.98 \cdot 10^3 \, Re_g^{-1.54} Re_l^{0.65} \tag{6}$$

where, for the gas and liquid phases, the Reynolds numbers are defined as:

$$Re_g = \frac{\rho_g J_g D}{\mu_g} \tag{7}$$

$$Re_l = \frac{\rho_l J_l D}{\mu_l} = \frac{4\,\Gamma}{\mu} \tag{8}$$

being Γ the liquid film mass flow rate per circumferential length unit, $\Gamma = \frac{\dot{m}}{\pi D}$.

Figure 21 displays a 3D comparison between the experimental data and the fitting plane provided by the correlation developed in the present study. A quantitative representation of the goodness-of-fit is displayed in Figure 22, in which a 2D graphic of the experimental data fitting line along with the new correlation are plotted. The new correlation leads to a good experimental data fitting, since almost they all are comprised by the error band of 10%, with a Pearson product-moment correlation coefficient of R^2=0.96.

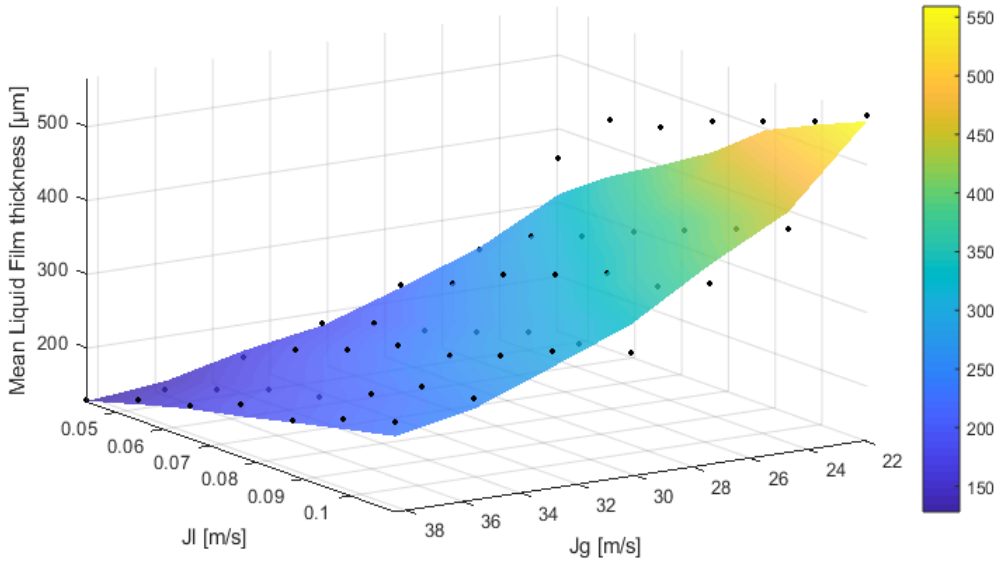

Figure 21. 3D graphic of the experimental data and the correlated fitting plane of the Mean Liquid Film Thickness versus the Superficial Gas and Liquid Velocities.

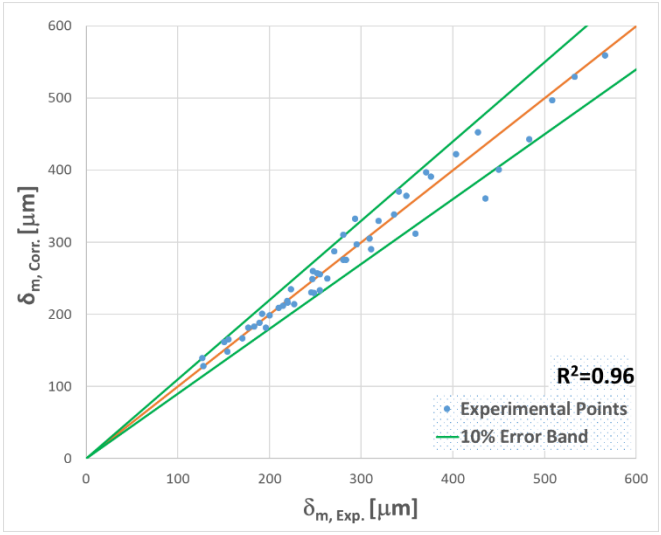

Figure 22. Comparison between the experimental data of the Mean Liquid Film Thickness and the correlated with the new expression developed in the current study.

An initial glance to the experimental data and their correlation shows the dependency of the mean liquid film thickness with superficial gas and liquid velocities. An upward trend in the mean liquid film thickness with the increase in the superficial liquid velocity is clearly shown, while the opposite tendency is observed with the rise in the superficial gas velocity values. Being the exponent of this term bigger than the one of the liquid in Eqn. (6), which lead to the conclusion that the gas phase dominates the behavior of this variable.

5.1.1.2. Comparison of the Experimental Data Against Mean Liquid Film Thickness Correlations

The whole experimental data series not only have been used to develop the correlations shown above, but also to test the performance of several of the most widely used correlations found in the literature. Table 6 displays the correlations used to estimate the values of the mean liquid film thickness as function of the experimental conditions, along with the correlation developed under the present study. Particularly, the displayed correlations are the Pan's

[Pan et al., 2015], Berna's [Berna et al., 2014], Fukano's [Fukano and Furukawa, 1998] and Henstock's [Henstock and Hanratty, 1976]. In Figures 23 and 24, these comparisons are shown in terms of superficial liquid and gas velocities for several tests run under this study.

Specifically, Figure 23 shows two examples of the dependency of the mean liquid film thickness as function of superficial liquid velocity for constant superficial gas velocity. While, the dependency of the mean liquid film thickness as function of superficial gas velocity for constant superficial liquid velocity is displayed in Figure 24. In relation to Figures 23 and 24, the above-mentioned trends are clearly shown, i.e., ascending tendency of the mean film thickness with the superficial liquid velocity and descending tendency with the superficial gas velocity. Highlight that all the displayed correlations provide values in quite close ranges to that of the experimental measurements for all the experimental data series.

The upward trend of the experimental data with superficial liquid velocity at constant superficial gas velocity is fairly well captured by all the correlations, as shown in Figure 23. Although, the correlation developed under the current study and Fukano's, capture more accurately the experimental trends. For all the experimental series, the new correlation is the most accurate one, except for the lowest superficial gas velocity measurements, in which Fukano's correlation better fits the four experimental points of lower superficial liquid velocity (Figure 23-A). Another possible way to come to the same conclusions is displayed in Figure 24. In this figure is shown that the new correlation is the one that better fit all the experimental data series, except the lowest value of Figure 24-A, for which any of the displayed correlations are inside the error bar of the experimental data point, being the Fukano's correlation the closest one. As explained above, only the lowest value of the superficial gas velocity are better captured by the Fukano's correlation, as displayed in Figure 23-A.

Table 6.Summary of correlations for the estimation of the Mean Liquid Film Thickness.

Reference	Correlation
Pan [Pan et al., 2015]	$\frac{\delta_m}{D} = 2.03\ Re_{lf}^{0.15}\ Re_g^{-0.6}$ $Re_{lf} = (1-E)\ \ Re_l$
Berna [Berna et al., 2014]	$\frac{\delta_m}{D} = 7.165\ Re_g^{-1.07}\ Re_l^{0.48}\left(\frac{Fr_g}{Fr_l}\right)^{0.24}$
Fukano [Fukano, 1998]	$\frac{\delta_m}{D} = 0.0594 \exp\left(-0.34\ Fr_g^{0.25} Re_l^{0.19} x^{*\,0.6}\right)$ $Fr_g = \frac{J_g}{\sqrt{g\,D}}\ ;\ x^* = \frac{J_g \rho_g}{J_g \rho_g + J_l \rho_l}$
Henstock [Henstock, 1976]	$\frac{\delta_m}{D} = \frac{6.59\,F}{(1+1400\,F)^{0.5}}$ (Vertical Flows) $F = \frac{1}{\sqrt{2}} \frac{Re_l^{0.5}}{Re_g^{0.9}} \frac{\mu_l}{\mu_g} \frac{\rho_g^{0.5}}{\rho_l^{0.5}}$

New Correlation	$\frac{\delta_m}{D} = 9.98 \cdot 10^3 \, Re_g^{-1.54} Re_l^{0.65}$	Eqn. (6)

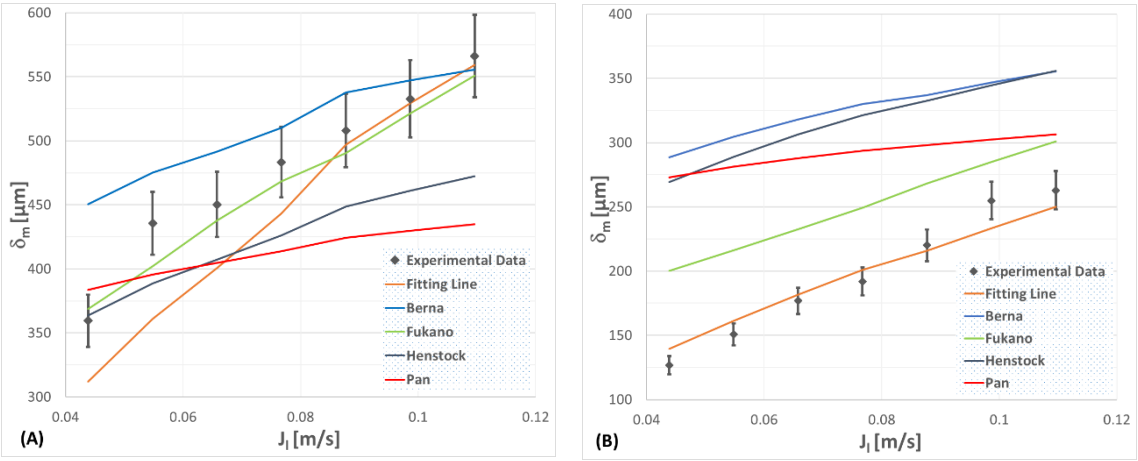

Figure 23. Experimental data of the Mean Liquid Film Thickness versus correlation curves as function of the Superficial Liquid Velocity with constant superficial gas velocity: (A) J_g=21.9 m/s; (B) J_g=35.6 m/s.

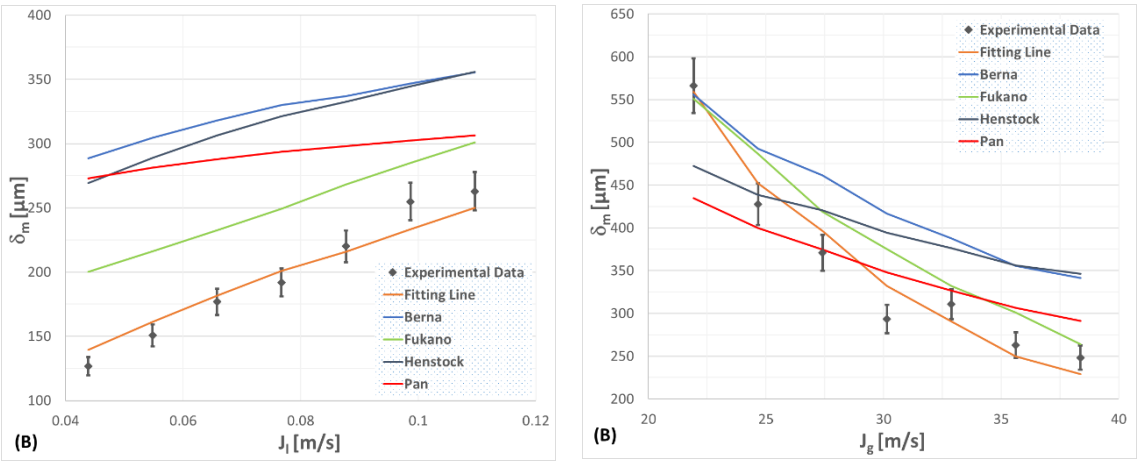

Figure 24. Experimental data of the Mean Liquid Film Thickness versus correlation curves as function of the Superficial Gas Velocity with constant superficial liquid velocity: (A) J_l=0.055 m/s; (B) J_l=0.11 m/s.

5.1.2. BASE LIQUID FILM THICKNESS

The wave base height or base film thickness, δ_b, is defined as the film thickness averaged value between DWs (Figure 2).

5.1.2.1. Correlation of the Base Liquid Film Thickness Measurements

From our experimental data, the same procedure used for the mean liquid film thickness has been followed for the estimation of the base liquid film thickness. Then, the correlation procedure has been the same as the one explained in section 5.1.1.1, i.e., use of non-dimensional numbers to correlate the base liquid film thickness in order to have a most general relationship. Being the new correlation:

$$\frac{\delta_b}{D} = 24.2 \, Re_g^{-1.2} Re_l^{0.6} \quad (9)$$

where both Reynolds numbers were defined in Eqn. (7) and Eqn. (8).

The experimental data points against the new correlation are displayed in Figure 25. In which can be shown that a good fitting of all the experimental data has been reached, since almost all are very close to the correlation's line. In fact, practically all the experimental points are contained into the ±10% error band, having a correlation coefficient of R^2=0.94.

As intuitively seems, the base liquid film thickness correlation and its dependency with dimensionless numbers is quite similar to that of the mean liquid film thickness, Eqns. (6) and (9). Being inversely proportional to the superficial gas velocity and directly proportional to that of the superficial liquid velocity. Additionally, the base film thickness correlation presents quite similar exponents for both dimensionless numbers to those of the mean liquid film thickness.

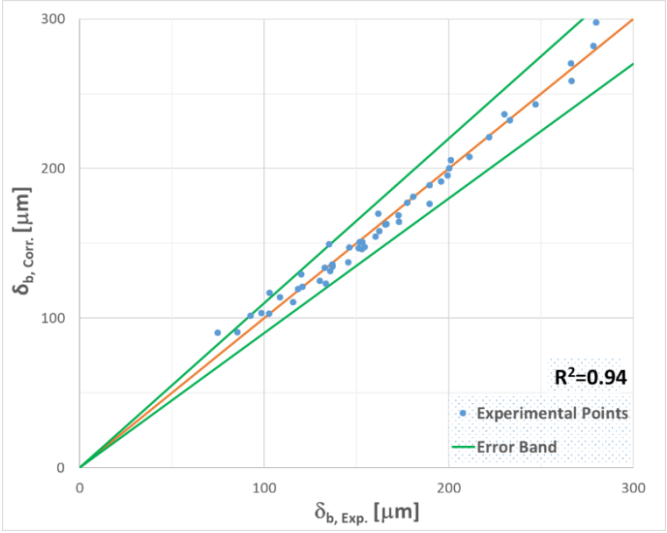

Figure 25. Comparison between the experimental data of the Base Liquid Film Thickness and the correlated with the new expression developed in the current study.

5.1.2.2. Comparison of the Experimental Data Against Base Liquid Film Thickness Correlations

As for the mean liquid film thickness, the experimental data series have been used to develop the base film thickness correlation and to test the performance of several correlations found in the literature (Table 7). Figures 26 and 27 display these comparisons in terms of superficial liquid and gas velocities.

Figures 26 and 27 display the comparison of the current data against the new expression proposed here and against well-known correlations found in research works. As shown in Figure 27, all three correlations capture the inverse dependency of the base film thickness with the superficial gas velocity. However, the upward trend with the superficial liquid velocity is not captured by any of them, only by the one presented in this paper. Schubring's correlation, as explained by the author, is a very simple expression developed originally for horizontal annular flows, which only considers the gas influence (which is the dominant term). Dobran's correlation is inversely proportional to the superficial liquid velocity, the opposite tendency to what is proposed here, which does not seem very logical because under the same gas flow rate, the increase in the liquid flow rate intuitively should lead to the increase in the liquid layer too, but this correlation lead to the opposite tendency.

To end this section, it should be highlighted that the correlation proposed in this work properly fits throughout the covered experimental range. Also, note that Schubring's correlation provides an approximate value in all cases (without capturing the influence of the liquid flow rate), while Dobran's correlation captures very well some experimental points, but is the most distant in others, added to its opposite trend versus the liquid flow rate.

Table 7. .Summary of correlations for the estimation of the Base Liquid Film Thickness.

Reference	Correlation
Dobran [Dobran, 1983]	$\frac{\delta_b}{D} = 140\ Gr_l^{0.2165}\ Re_c^{-1.35}$ (1) $Gr_l = \frac{g\ D^3 \rho_l\ (\rho_l - \rho_c)}{\mu_l^2}$ $Re_c = \frac{J_c\ \rho_c\ D}{\mu_g}$ $J_c = J_g + E\ J_l$ $\rho_c = \alpha\ \rho_g + (1-\alpha)\rho_l$ $\alpha_c = \frac{J_g}{J_g + J_l E}$
Schubring [Schubring, 2009]	$\frac{\delta_b}{D} = 4.8\ Re_g^{-0.6}$
New Correlation	$\frac{\delta_b}{D} = 24.2\ Re_g^{-1.2} Re_l^{0.6}$ Eqn. (9)

(1) Originally Dobran estimated the base film thickness in terms of nondimensional film thickness $\left(\delta_b^+ = \frac{\rho_l \delta_l u^*}{\mu_l}\right)$ and diameter $\left(D^+ = \frac{\rho_l D u*}{\mu_l}\right)$, but the quotient of these nondimensional variables simplifies to $\frac{\delta_b}{D}$.

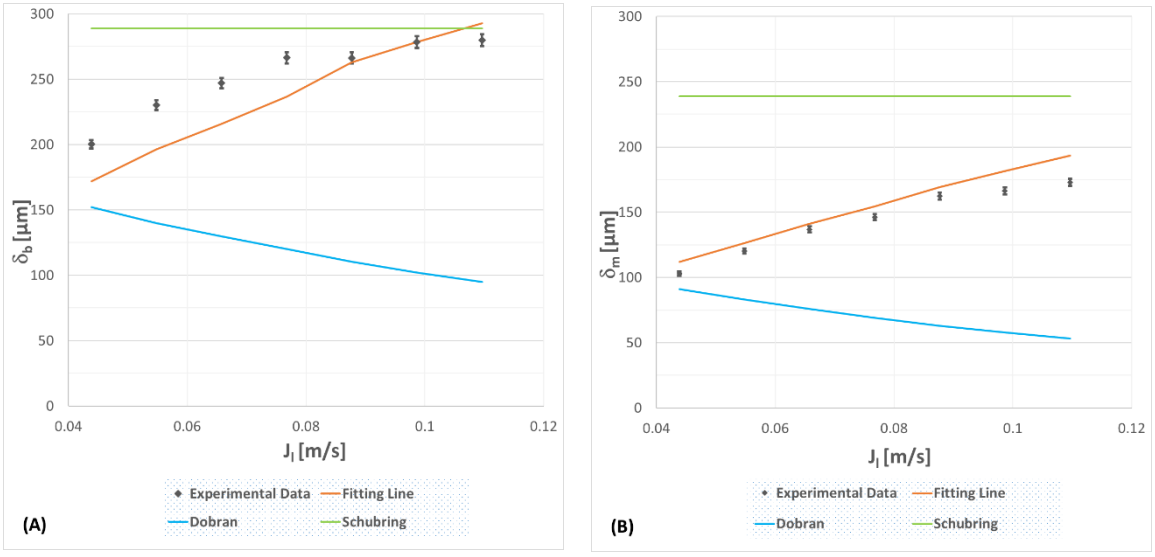

Figure 26. Experimental data of the Base Liquid Film Thickness versus correlation curves as function of the Superficial Liquid Velocity with constant superficial gas velocity: (A) J_g=21.9 m/s; (B) J_g=30.1 m/s.

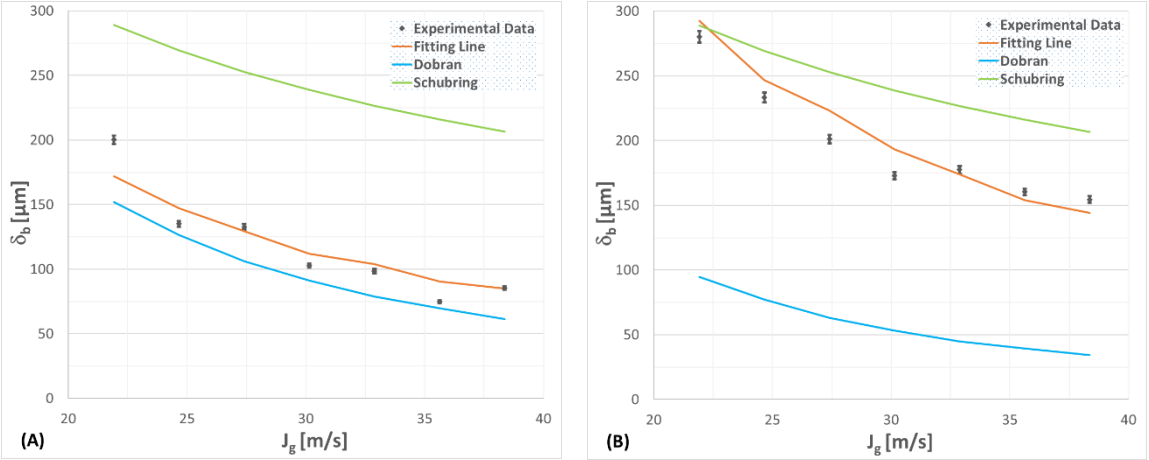

Figure 27. Experimental data of the Base Liquid Film Thickness versus correlation curves as function of the Superficial Gas Velocity with constant superficial liquid velocity: (A) J_l=0.044 m/s; (B) J_l=0.11 m/s.

5.2. Analysis of the Disturbance Wave

Along this section the major characteristics of the DWs are estimated. Specifically, wave amplitudes and frequencies are correlated in terms of the experimental conditions, in order to characterize the gas-liquid interfacial waves. The adjustment procedure to estimate the amplitude and frequency of the DWs has also been carried out in terms of dimensionless numbers, as for the previous variables.

5.2.1. DISTURBANCE WAVE AMPLITUDE

The DW amplitude or wave roughness height is usually defined as the distance between the DW peak and the base film.

5.2.1.1. Correlation of the Disturbance Wave Amplitude Measurements

Proceeding as in previous sections, dimensionless numbers have been used to correlate the disturbance wave amplitudes measurements. Finally, arriving at the following correlation:

$$\frac{A_{DW}}{D} = 7.33\, Re_g^{-0.73} Re_l^{0.26} \qquad (10)$$

defining the gas and liquid Reynolds numbers as in Eqn. (7) and Eqn. (8).

The fitting correlation, Eqn. (10), and the experimental data are displayed in Figure 28. An acceptable correlation is achieved, since almost all points are between the ±10% error bands, with a value for correlation coefficient of R^2=0.79.

The tendency found for the wave amplitude is similar to the one shown for both variables related to the film thickness. An upward trend has been found in the wave amplitude with the increase of the superficial liquid velocity, while the opposite tendency has been observed for the superficial gas velocity.

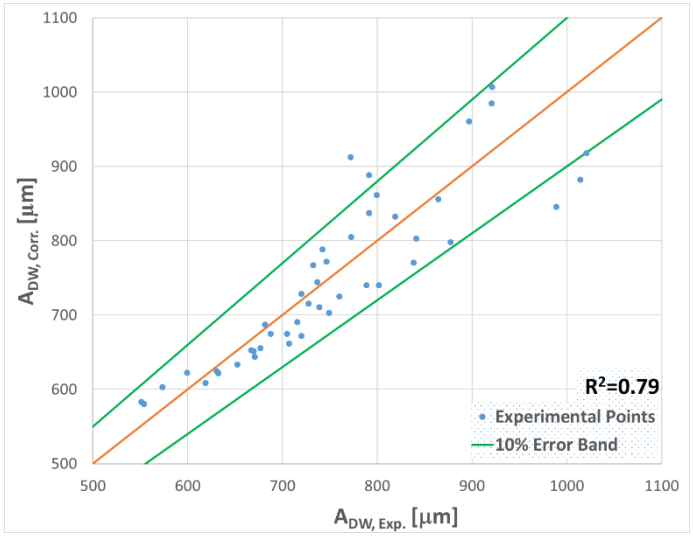

Figure 28. Comparison between the experimental data of the Disturbance Wave Amplitudes and correlated with the new expression developed in the current study.

5.2.1.2. Comparison of the Experimental Data Against Wave Amplitude Correlations

As mentioned in previous subsections, all the experimental data have been used to develop the correlation shown above and also to test its performance against several of the most widely used correlations (Table 8). As for the previous cases, a reduced number of expressions to estimate the DW amplitude are available. Figures 29 and 30 display the experimental data, their fitting correlation and their comparisons against Chandrasekhar's [Chandrasekhar, 1981], Han's [Han et al., 2006] and Holowach's [Holowach et al., 2002] expressions, all of them are shown in terms of superficial liquid and gas velocities.

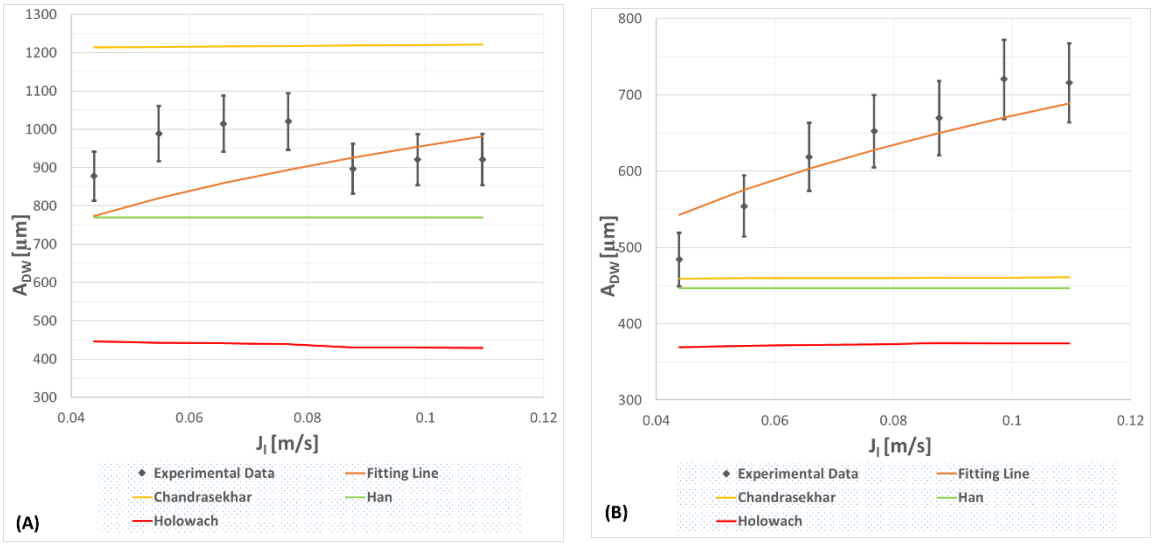

Figure 29. Experimental data of the Disturbance Wave Amplitudes versus correlation curves as function of the Superficial Liquid Velocity with constant superficial gas velocity: (A) J_g=21.9 m/s; (B) J_g=35.6 m/s.

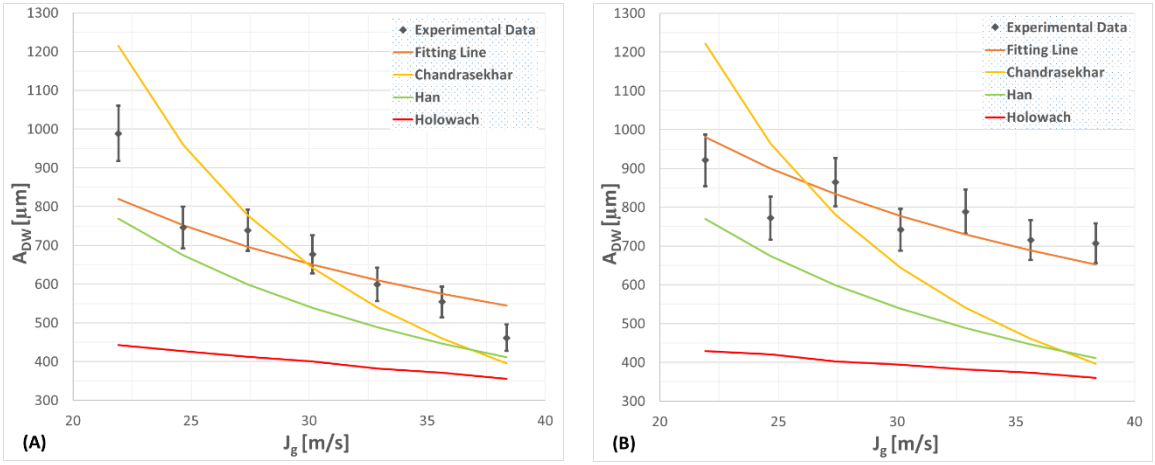

Figure 30. Experimental data of the Disturbance Wave Amplitudes versus correlation curves as function of the Superficial Gas Velocity with constant superficial liquid velocity: (A) J_l=0.055 m/s; (B) J_l=0.11 m/s.

Table 8. .Summary of correlations for the estimation of the Disturbance Wave Amplitude.

Reference	Correlation
Chandrasekhar [Chandrasekhar, 1981]	$$A_{DW} = 3\,\pi \frac{\left(1+\frac{\rho_g}{\rho_l}\right)\sigma_l}{\rho_g (u_g - u_l)^2}$$
Han [Han et al., 2006]	$$\frac{A_{DW}}{D} = 4 \cdot 10^3\, Re_g^{-1.12}$$
Holowach [Holowach et al., 2002]	$$A_{DW} = \frac{\sqrt{2} C_W \mu_l}{\sqrt{\rho_l \tau_i f_{li}}}$$ $$C_W = \begin{cases} 0.028\, N_\mu^{-\frac{4}{5}} \; for \; N_\mu \le \frac{1}{15} \\ 0.25 \qquad for \; N_\mu > \frac{1}{15} \end{cases}$$ $$N_\mu = \frac{\mu_l}{\sqrt{\rho_l \sigma \sqrt{\frac{\sigma}{g\,\Delta\rho}}}}$$ $$\tau_i = \frac{1}{2} f_{gi} \rho_g (u_g - u_l)^2$$ $$f_{gi} = \frac{0.079}{Re_g^{0.25}}\left(1 + 300\,\frac{\delta}{D}\right)$$ $$\sqrt{f_{li}} = \begin{cases} 3.73\, Re_{lf}^{-0.47} \; for\; 2 < Re_{lf} < 100 \\ 1.962\, Re_{lf}^{-\frac{1}{3}} \; for\; 100 < Re_{lf} < 1000 \\ 0.735\, Re_{lf}^{-0.19} \; for\; 1000 < Re_{lf} \end{cases}$$
New Correlation	$$\frac{A_{DW}}{D} = 7.33\, Re_g^{-0.73} Re_l^{0.26}$$ Eqn. (10)

Chandrasekhar's expression takes into account the Kelvin-Helmholtz instability (K-H) in order to estimate the DW amplitudes, in which the DWs are caused by the relative motion between the two fluids. Holowach's expression is based on Ishii and Grolmes' methodology. In Holowach's model, the wave amplitudes are mainly determined by the gas-liquid interfacial shear stress and a dimensionless parameter that accounts for the surface tension forces (C_W, originally proposed by Ishii and Grolmes [Ishii and Grolmes, 1975]). The Han's experimental work was carried out in a vertical pipe of 9.525 mm of inner diameter and his correlation is based on a force balance (forces trying to maintain a smooth surface versus forces trying to disturb this flat surface), through the expression of this balance in terms of dimensionless numbers, specifically the gas Reynolds number (inertial versus viscous forces).

Figures 29 and 30 display the comparison between the experimental data and the correlation curves. A slight slope has been found with the variation of the liquid flow rate, which is not shown in the rest of the analyzed correlations. To corroborate this direct proportionality, between the wave amplitude and the liquid flow rate, further investigations should be carried out. Regarding the influence of the gas flow rate, it should be noted that Holowach's expression underestimates the wave amplitudes for all the covered experimental range. Chandrasekhar's expression passes from overestimation to underestimation of the wave amplitudes as the gas flow rate increases. Meanwhile the Han's expression underestimates the wave amplitudes along the whole measurement range, being very close in the lower gas flow rates values, moving away as the gas flow rates increase, although at an acceptable difference (maximum difference of about 30%). The correlation proposed in the present study captures not only the tendency of the experimental data with the superficial gas and liquid velocities, but also their magnitude. As shown in Figure 28, almost all the experimental data are within the ±10% error band.

5.2.2. DISTURBANCE WAVE FREQUENCY

The DW frequency is the second variable related with the characterization of the interfacial waves which has been analyzed. The wave frequency can be defined as the inverse of a time period between successive waves, i.e., the number of large amplitude waves per second.

5.2.2.1. Correlation of the Disturbance Wave Frequency Measurements

We proceed for the adjustment of the experimental frequency data in the same way than that of the DWs amplitude adjustment. The only difference is the use of the Strouhal number to adimensionalize the DW frequency. Procedure that finally leads to the following expression:

$$St_l = 1.074 \cdot 10^2 \, Re_g^{0.17} Re_l^{-0.55} \tag{11}$$

where St_l is the liquid Strouhal number, defined as:

$$St_l = \frac{v_{DW} D}{J_l} \tag{12}$$

while, the gas and liquid Reynolds numbers were defined in Eqns. (7) and (8).

The fitting of the new correlation with the wave frequency experimental data is displayed in Figure 31. The figure displays that the new correlation leads to a reasonably good fitting of all experimental data, since almost all of them are nearby the correlation's line. In fact, as in the previous cases, almost all are included by the ±10% error band, having a correlation coefficient of R^2=0.86.

The tendency found for the wave frequency is not the same to that shown for the rest of variables analyzed until now. In this case, both mass flows lead an increase in the wave frequency, i.e., upward trends have been found for the DWs frequencies with the increase of both superficial velocities. In spite of liquid Reynolds number has a negative exponent, but as the Strouhal number has the superficial liquid velocity in the denominator, then, finally the superficial liquid velocity exponent is +0.45.

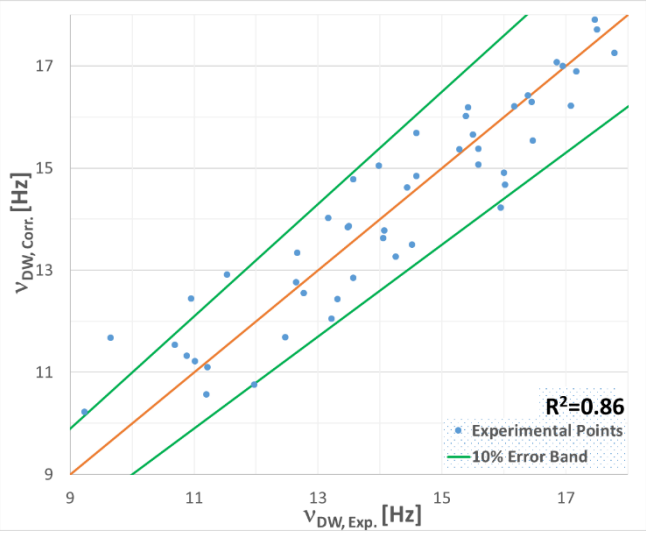

Figure 31. Comparison between the experimental data of the Disturbance Wave Frequencies versus the calculated from the correlation developed in the current study.

5.2.2.2. Comparison of the Experimental Data Against Wave Frequency Correlations

As in previous sections, all the experimental data have been used to develop a new correlation and to test its performance against several extensively used correlations found in the literature (Table 9). Figures 32 and 33 display the experimental data, their fitting correlation and their comparisons against Azzopardi's [Azzopardi, 2006], Berna's [Berna et al., 2014], Sawant's [Sawant et al., 2008] and Sekoguchi's [Sawant et al., 2008] expressions, all of them are expressed in terms of superficial liquid and gas velocities.

With regard to the absolute frequency values, Sawant's and Sekoguchi's expressions are the ones that predict lower values throughout the covered experimental range (about half of the wave frequency measurements), as shown in Figures 32 and 33. Azzopardi's expression adequately predicts some experimental points but is far away from others (remember the opposite trend with the superficial liquid velocity with regard to the experimental data and the rest of expressions). Berna's correlation captures most of the experimental points in a fairly precise way, overestimating the wave frequency measurements when the gas velocity is high and the liquid velocity is low, as clearly shown in Figures 32A and 33A (values of the correlated frequency which almost double the

experimental measurements). Certainly, the correlation proposed in this work is the one that best fits the experimental values of the present study.

Table 9. .Summary of correlations for the estimation of the Disturbance Wave Frequency.

Reference	Correlation
Azzopardi [Azzopardi, 2006]	$St_l = 0.25\ X^{-1.2}$ $X = \sqrt{\frac{\rho_l J_l^2}{\rho_g J_g^2}}$
Berna [Berna et al., 2014]	$St_{gl} = 1.38 \cdot 10^{-2}\ Re_g^{0.53} Re_l^{-0.48} Eo^{0.27} \left(\frac{\rho_g}{\rho_l}\right)^{0.14} C_W^{0.68}$ $St_{gl} = \frac{\nu_{DW} D}{\sqrt{J_g J_l}}$ $Eo = \frac{g\ D^2(\rho_g - \rho_l)}{\sigma}$ $C_W = \begin{cases} 0.028\ N_\mu^{-\frac{4}{5}} & for\ \ N_\mu \leq \frac{1}{15} \\ 0.25 & for\ \ N_\mu > \frac{1}{15} \end{cases}$ $\mathrm{N}_\mu = \frac{\mu_l}{\sqrt{\rho_l \sigma \sqrt{\frac{\sigma}{g\ \Delta\rho}}}}$
Sawant [Sawant et al., 2008]	$\mathrm{St}_g = 0.086\ Re_l^{0.27} \left(\frac{\rho_l}{\rho_g}\right)^{-0.64}$ $St_g = \frac{\nu_{DW} D}{J_g}$
Sekoguchi [Sawant et al., 2008]	$\mathrm{St}_g = f_1(Eo) f_2(Re_l, Fr_g)$ $Fr_g = \frac{J_g}{\sqrt{g\ D}}$ $f_1(Eo) = Eo^{-0.5}[0.5\ Ln(Eo) - 0.47]$ $f_2(Re_l, Fr_g) = 0.076\ Ln\left(\frac{Re_l^{2.5}}{Fr_g}\right) - 0.051$
New Correlation	$St_l = 1.074 \cdot 10^2\ Re_g^{0.17} Re_l^{-0.55}$ Eqn. (11)

Finally, to end the section, to highlight the existing scattering found when comparing the experimental data against the available correlations. Regarding the dependence on the superficial liquid velocity for constant superficial gas velocities (Figure 32), there is a greater disparity of wave frequency predictions. There is an inverse tendency with superficial liquid velocity of the Azzopardi's

correlation, while there is a direct proportionality for the rest of the expressions, except in Berna's expression, in which there is a practically flat trend with the superficial liquid velocity. The largest slope is provided by the expression proposed in the present document. Regarding the superficial gas velocity dependency (Figure 33), all the expressions and the experimental data have a direct proportionality of the wave frequency with the superficial gas velocities, with Berna's correlation having the highest slope, while Sawant's and Sekoguchi's correlations have the lowest ones.

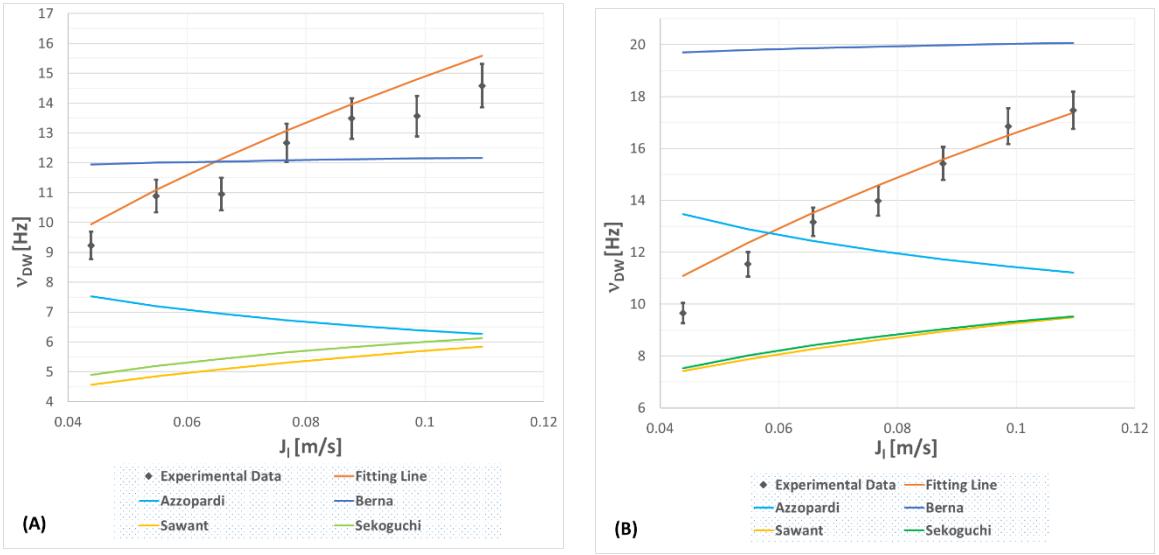

Figure 32. Experimental data of the Disturbance Wave Frequencies versus correlation curves as function of the Superficial Liquid Velocity with constant superficial gas velocity: (A) J_g=21.9 m/s; (B) J_g=35.6 m/s.

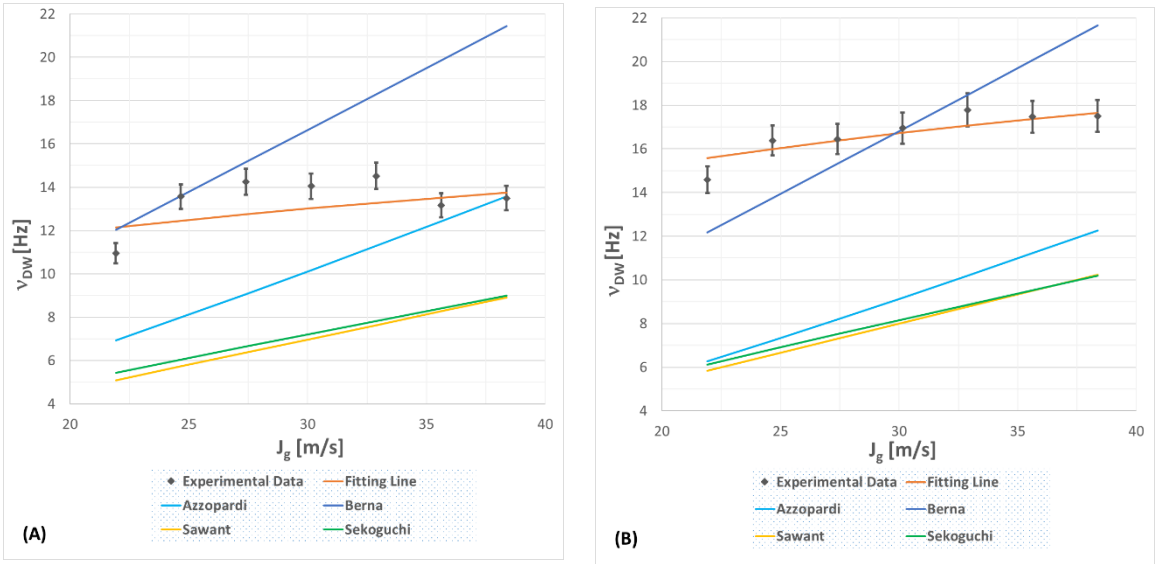

Figure 33. Experimental data of the Disturbance Wave Frequencies versus correlation curves as function of the Superficial Gas Velocity with constant superficial liquid velocity: (A) J_l=0.066 m/s; (B) J_l=0.11 m/s.

6. CONCLUSIONS

A specially designed conductivity probe has been built in order to study vertical upward co-current two-phase gas-liquid flows. This process includes the

design and construction of the electronic circuit and of the conductance probe port, ending with the sensor calibration procedure. With the aim to acquire data of liquid film thicknesses at high speed and with high precision, 10^5 samples per second have been stored during 60 seconds per experimental run. The raw data have been treated through MATLAB code, and from these filtered data, several variables have been studied in order to characterize the gas-liquid interface and the liquid layer. Specifically, the base liquid film thickness, the mean liquid film thickness, the disturbance wave amplitude and the disturbance wave frequency have been estimated from the treated data. During all the experiments, the pressure at the upper part of the facility was kept at atmospheric conditions, while the water and air temperatures were kept constant. Forty nine test runs have been made (seven air flows and seven water flows) in an approximately 5 meters vertical pipe of 44 mm of inner diameter. The variation range of superficial air and water velocities covered from 21.9 to 38.4 m/s and from $4.4 \cdot 10^{-2}$ to $11.0 \cdot 10^{-2}$ m/s, respectively.

The way in which the thin liquid film evolves has been studied, in particular, the wavy gas-liquid interface and the thickness of the liquid layer have been characterized. Taking the experimental data as a starting point, the four variables under study have been correlated. Comparisons of the experimental data and the calculations provided by the developed correlations have been carried out for each variable, along with the comparison against several of the existing correlations found in the literature. This comparison has been made through the expression of these variables in terms of dimensionless numbers, usually the gas and liquid Reynolds numbers (quotient of inertial versus viscous forces). These adjustments have been made in this way because the balance of these forces is the dominant phenomenon which takes place on the gas-liquid interface, which lead to its wavy form. This force balance consists of an equilibrium between the ones that are trying to maintain a smooth surface (viscous forces) versus the ones that are trying to disturb this flat surface (inertial forces).

The major conclusions related with the evolution of the liquid film thickness (both mean and base) are the direct proportionality with the liquid flow rate and the inverse proportionality with the gas flow rate, being this last variable the dominant. The same tendency, as explained in the previous lines, has been measured for the disturbance wave height, while a direct proportionality for both superficial velocities has been observed in the wave frequency data.

The mean liquid film thickness ranges from slightly over 100 μm up to almost 600 μm. The minimum thickness value was measured for the highest value of the superficial gas velocity (38.4 m/s) and the lowest value for the superficial water velocity ($4.4 \cdot 10^{-2}$ m/s), while the highest was measured for the lowest value of the superficial gas velocity (21.4 m/s) and the highest for the superficial water velocity ($11.0 \cdot 10^{-2}$ m/s). Whereas for the base liquid film thickness measurements, they have values of approximately a bit more than half of the value of the mean liquid film thickness.

With regard to the disturbance wave amplitudes, they range from almost 350 μm to near 1000 μm, for highest-lowest and lowest-highest superficial gas- liquid velocities respectively, being this tendency similar to that of the film thicknesses. For the disturbance wave frequencies, the range varies between 9 and 17.5 Hz approximately, with an increasing tendency with superficial gas-liquid velocities.

For all the studied variables, there is a significant scattering among the predictions of the compared correlations and the experimental data. This scattering has been particularly significant for the wave frequency data. But, in spite of this dispersion, it can be concluded that all the studied variables can be estimated with an adequate precision.

We must finalize this experimental work by emphasizing a major aspect. The development of four new correlations, which characterize the key variables of vertical upward co-current annular flows. The proposed correlations produce a noticeable improvement, compared with those found in the open literature for the experimental range covered in this study. This enhancement has been displayed throughout the whole section 5, in which the 4 new correlations developed during this work have been tested against many of the most widely used expressions. In particular, correlations to estimate the base and mean liquid film thickness, the wave amplitude and frequency have been developed and tested along this work.

ACKNOWLEDGEMENTS

The authors are indebted to the plan of I+D support of the EXMOTRANSIN project ENE2016-79489-C2-1-P.

REFERENCES

- Alekseenko S., Antipin V., Cherdantsev A., Kharlamov S., Markovich D., "**Two-Wave Structure of Liquid Film and Wave Interrelation in Annular Gas-Liquid Flow with and without Entrainment**". Physics of Fluids, Vol. 21 Nº1, Ner 061701 (2009).
- Alekseenko S., Antipin V., Cherdantsev A., Kharlamov S., Markovich D., "**Investigation of Waves Interaction in Annular Gas-Liquid Flow Using High-Speed Fluorescent Visualization Technique**". Microgravity Science Technology, Vol. 20 Nº1, pp .271 (2008).
- Azzopardi B. J., **"Gas-Liquid Flows**". Begell House Inc., New York (2006).
- Azzopardi B. J., **"Drops in annular two-phase flow"**. International Journal of Multiphase Flow, Vol. 23, pp. 1-53 (1997).
- Azzopardi B. J., **"Disturbance wave frequencies, velocities and spacing in vertical annular two-phase flow"**. Nuclear Engineering and Design, Vol. 92, pp. 121-133 (1986).
- Belt R.J., Van't Westende J. M.C., Prasser H.M., Portela L.M., "**Time spatially resolved measurements of interfacial waves in vertical annular flow**". International Journal of Multiphase Flow, Vol. 36, pp. 570-587 (2010).
- Berna C., Escrivá A., Muñoz-Cobo J.L., Herranz L.E., **"Review of droplet entrainment in annular flow: interfacial waves and onset of entrainment"**. Progress in Nuclear Energy, Vol. 74, p.p. 14-43 (2014).
- Berna C., Escrivá A., Muñoz-Cobo J.L., Herranz L.E., **"Review of droplet entrainment in annular flow: characterization of the entrained droplets"**. Progress in Nuclear Energy, Vol. 79, p.p. 64-86 (2015).
- Chandrasekhar S., "**Hydrodynamic and Hydromagnetic Stability**". Oxford University Press (1981).
- Chen C., Gao P.-Z., Tan S.-C., Chen H.-Y., Xu C., Yu Z.-T., **"Theoretical calculation of the characteristics of annular flow in a rectangular narrow channel"**. Annals of Nuclear Energy, Vol. 85, p.p. 259-270 (2015).
- Cioncolini A., Thome J.R., "**Pressure drop prediction in annular two-phase flow in macroscale tubes and channels**". International Journal of Multiphase Flow, Vol. 89, pp. 321-330 (2017).
- Collier J.G., Thome J.R., "**Concective Boiling and Condensation**". Clarendon Press, Oxford Science Publications (1994).
- Dasgupta A., Chandraker D.K., Kshirasagar S., Raghavendra Reddy B., Rajalakshimi R., Nayak A.K., Walker S.P., Vijayan P.K., Hewitt G.F., "**Experimental investigation on**

dominant waves in upward air-water two-phase flow in churn and annular regime", Experimental Thermal and Fluid Science, Vol. 81, pp. 147-163 (2017).

- De Jong P., Gabriel K. S., **"A preliminary study of two-phase annular flow at microgravity: experimental data of film thickness"**. International Journal of Multiphase Flow, Vol. 23, pp. 1203-1220 (2003).
- Dobran F., "**Hydrodynamic and heat transfer analysis of two-phase annular flow with a new liquid film model of turbulence**". International Journal of Heat and Mass Transfer, Vol. 26, No. 8, pp. 1159-1171 (1983).
- Fukano T., Furukawa T., "**Prediction of the Effects of Liquid Viscosity on Interfacial Shear Stress and Frictional Pressure Drop in Vertical Upward Gas-Liquid Annular Flow**". International Journal of Multiphase Flow, Vol. 24, No 4, pp. 587-603 (1998).
- Hall-Taylor N.S., Hewitt G.F., Lacey P.M.C., **"The motion and frequency of large disturbance waves in annular two-phase flow of air-water mixtures"**. Chem. Eng. Sci. Vol. 18, pp. 537-552 (1963).
- Han H., Zhu Z., Gabriel K., **"A study on the effect of gas flow rate on the wave characteristics in two-phase gas-liquid annular flow"**. Nuclear Engineering and Design, Vol. 236, pp. 2580–2588 (2006).
- Hanratty T.J., Hershman, A., **"Initiation of roll waves"**. Am. Inst. Chem. Eng. Journal, Vol. 7, pp. 488 (1961).
- Henstock W.H., Hanratty T.J., "**The interfacial drag and the height of the wall layer in annular flows**". AIChE Journal, Vol.22 N.6, pp. 990-1000 (1976).
- Hewitt G.F., Hall-Taylor N.S., **"Annular Two-phase Flow"**. Pergamon Press, Oxford, pp. 136-139 (1970).
- Holowach M.J., Hochreiter L.E., Cheung F.B., "**A model for droplet entrainment in heated annular flow**". International Journal of Heat and Fluid Flow, Vol. 23, pp. 807-822 (2002).
- Ishii M., Grolmes M.A., "**Inception Criteria for Droplet Entrainment in Two-Phase Concurrent Film Flow**". AIChE Journal, Vol. 21 p. 308-318 (1975).
- Kim S.-M., Mudawar I., **"Theoretical model for local heat transfer coefficient for annular flow boiling in circular mini/micro-channels"**. International Journal of Heat and Mass Transfer, Vol. 73, pp. 731–742 (2014).
- Kim S.-M., Mudawar I., **"Theoretical model for annular flow condensation in rectangular micro-channels"**. International Journal of Heat and Mass Transfer, Vol. 55, pp. 958–970 (2012).
- Kolev N.I., "**Multiphase Flow Dynamics 5. Nuclear Thermal Hydraulics**". Springer, ISBN 978-3-319—15155-7 (2015).
- Lahey R.T. Jr., Moody F.J., "**The Thermal-Hydraulics of a Boiling Water Nuclear Reactor**". American Nuclear Society, ISBN 0-89448-037-5 (1993).
- Muñoz-Cobo J.L:, Chiva S., Méndez S., Monrós G., Escrivá A., Cuadros J.L., **"Development of Conductivity Sensors for Multi-Phase flow Local Measurements at the Polytechnic University of Valencia (UPV) and University Jaume I of Castellon (UJI)"**. Sensors 2017, 17, 1077; doi:10.3390/s17051077 (2017).
- Pan L.-M., He H., Hibiki T., Ishiii M., "**Experimental study and modeling of disturbance wave height of vertical annular flow**". International Journal of Heat and Mass Transfer, Vol. 89, pp. 165-175 (2015).
- Paras S.V., Karabelas A.J., **"Properties of the Liquid Layer in Horizontal Annular Flow"**. International Journal of Multiphase Flow, Vol. 17, No 4, pp. 439-454 (1991).
- Rodriguez D.J., "**Characterization of bubble entrainment, interfacial roughness and the sliding bubble mechanism in horizontal annular flow**". PhD. Thesis University of Wisconsin-Madison (2004).
- Sawant P., Ishii M., Hazuku T., Takamasa T., Mori M., "**Properties of Disturbance Waves in Vertical Annular Two-phase Flow**". Nuclear Engineering and Design, Vol. 238, pp. 3528-3541 (2008).
- Schubring D., Shedd T.A., "**Wave behavior in horizontal annular air-water flow**". International Journal of Multiphase Flow, Vol. 34, pp. 636-646 (2008).
- Schubring D., "**Behavior interrelationships in annular flow**". PhD. Thesis University of Wisconsin-Madison (2009).
- Setyawan A., Indarto I., Deendarlianto. A., "**The effect of the fluid properties on the wave velocity and wave frequency of gas-liquid annular two-phase flow in a horizontal pipe**". Experimental Thermal and Fluid Science, Vol. 71, pp. 25-41 (2016).

- Su G., Gou J., Qiu S. Yang X., Jia D., **"Theoretical calculation of annular upward flow in a narrow annuli with bilateral heating"**. Nuclear Engineering and Design, Vol. 225, pp. 219-247 (2003a).
- Su G., Gou J., Fukuda K., Jia D., **"A theoretical model of annular upward flow in a vertical annulus gap"**. Journal of Nuclear Science and Technology, Vol. 40, No. 1, pp. 1-11 (2003b).
- Tiwari R., Damsohn M., Prasser H.M., Wymann D., Gossweiler C., **"Multi-range sensors for the measurement of liquid film thickness distributions based on electrical conductance"**. Flow Meas. Instrum., Vol. 40, pp. 124–132 (2014).
- Todreas N.E., Kazimi M.S., **"Nuclear Systems I: Thermal Hydraulic Fundamentals"**. Taylor & Francis, ISBN 1-56032-051-6 (1993).
- UNE-EN ISO 4022, **"Materiales metálicos sinterizados permeables. Determinación de la permeabilidad a los fluidos (ISO 4022:1987)"**. AENOR, Comité Técnico AEN/CTN 96 Materiales sinterizados y sus materias primas (2007).
- Wallis G.B., **"One-dimensional Two-phase Flow"**. McGraw-Hill, Inc, New York, USA. (1969).
- Wayne C., **"The Interfacial Characteristics of Falling Film Reactors"**. Ph.D. Thesis, University of Nottingham, Nottingham, UK (2001).
- Zhao Y., Markides C.N., Matar O.K., Hewitt G.H., **"Disturbance wave development in two-phase gas–liquid upwards vertical annular flow"**, International Journal of Multiphase Flow 55, pp. 111–129 (2013).